2D WS_2 Photodetectors for Excitonic Light Absorption

MSc Thesis

Tom Hoekstra

Van der Waals-Zeeman Institute
University of Amsterdam
24th August 2021

Daily supervisor: Ludovica Guarneri MSc
Supervisor: Dr. Jorik van de Groep
Examiner: Dr. Peter Schall

Abstract

Photodetectors are semiconductor-based devices that convert absorbed photons into electrical signals and thereby retrieve the multi-dimensional information carried by light. Conventional photodetectors have only limited modulation potential for the optical responsivity, thus there is an ongoing search for novel materials and device architectures. The strongest modulation of a material's optical properties is achieved by manipulating excitons. However, in conventional semiconductors, excitons have low binding energies of $\sim$ 5 meV and are therefore thermally unstable. In contrast, excitons in monolayer tungsten disulphide (WS_2) have binding energies up to 0.71 eV and dominate the room-temperature optical response. Presently, it is still unclear which mechanism governs the dissociation of excitons into free charge carriers for efficient photodetection, and how this process can be manipulated to realise tuneable nanoscale photodetectors. To study this, we fabricate two-dimensional (2D) WS_2 photodetectors by mechanically exfoliating bulk WS_2 and deterministically transferring nanolayers onto an oxidised Si substrate. Using e-beam lithography, we fabricate contact electrodes on the WS_2 nanolayers. To characterise the photodetectors, we build a photocurrent mapping and spectroscopy setup, with precise control over the excitation power, wavelength and linear polarisation. The setup is integrated with a commercial confocal microscope to achieve diffraction-limited spatial resolution and high stability. We benchmark the setup with Mie-resonant Si NW array photodetectors and achieve excellent agreement with simulations. Lastly, we study the 2D WS_2 photodetectors and conclude that the photocurrent is generated in the substrate and that the excitons are suppressed in the WS_2 channels. Future work should aim to tackle these problems and address the research question by measuring the quantum efficiency of 2D WS_2 photodetectors.

Contents

Chapter 1

Introduction

Photodetectors are semiconductor-based devices that convert absorbed photons into electrical signals and thereby retrieve the multi-dimensional information carried by light, such as the intensity, wavelength or polarisation. Nowadays, this is a mature technology with applications such as electro-optical displays, optical communication, and remote sensing [1]. However, photodetectors based on conventional bulk semiconductors are limited by the material's properties. For instance, Silicon (Si) photodetectors are brittle, opaque, and reliant on thick channels and require external filters and optical elements to measure colour or polarisation. This makes them unsuited for up-and-coming technologies such as wearable electronics. Therefore, it is not surprising that there is an ongoing search for novel materials and device architectures to go beyond the limitations of current-day photodetectors.

Recently, there has been much activity aimed at semiconductor nanostructures, which exploit optical Mie resonances to dramatically enhance the light-matter interaction [2]. Si nanowires can trap light in circulating orbits by multiple total internal reflections, resulting in resonant absorption and scattering of the light. The resonance wavelength can be controlled by the nanowire geometry. This can be formulated as an intuitive, approximate resonance condition $p(\lambda/n) \approx 2\pi r$, where p is a positive integer, λ the free space illumination wavelength, n is the nanowire's refractive index and r its radius. As such, resonant semiconductor nanostructures enable the design of colour and polarisation-sensitive photodetectors, without the need for external filters. When Si nanowires are placed in each other's vicinity, coupling of the resonant

modes can be used to control spectral, polarisation-dependent [3], and even angle-dependent absorption and scattering [4]. However, leveraging Mie resonances for actively tuneable devices proves challenging, because they are fixed in the fabrication stage and offer only weak electrical tuneability.

Naturally, this raises the question what other resonances can be harnessed to realise actively tuneable photodetectors. From decades of research on optical modulation, it is clear that the strongest modulation of a material's optical properties is achieved by manipulating excitons, i.e. photoexcited electron-hole pairs bound by the Coulomb force [5]. Resonant excitation of excitons can give rise to sharp absorption features below the bandgap of a semiconductor. However, exciton binding energies tend to be small ($\sim$5 meV) in bulk semiconductors and Mie resonant nanostructures, due to dielectric screening of the Coulomb interaction. Quasi-2D systems such as gallium arsenide (GaAs) or gallium nitride (GaN) quantum wells achieve slightly larger exciton binding energies ($\sim$10 meV) due to their reduced dimensionality [6]. Nevertheless, excitonic features are largely absent in the room-temperature optical spectra of bulk and quasi-2D systems.

Since the isolation of two-dimensional (2D) semiconductors in 2005 [7], considerable efforts have been made to investigate the exciton physics in these natural quantum wells. In 2010, a class of 2D materials called transition metal dichalcogenides (TMDCs) were shown to undergo an indirect-to-direct bandgap transition when thinning from bulk to a single unit-cell thick layer, with strong photoluminescence emission and enhanced absorption at the exciton resonance [8]. In these natural quantum wells, the Coulomb interaction between electrons and holes is one to two orders of magnitude stronger than in GaAs or GaN quantum wells [9]. Consequently, the excitons in monolayer TMDCs have extremely large binding energies. For instance, the exciton binding energy in monolayer tungsten disulphide (WS_2) reaches up to 0.71 eV [10], dominating the optical response even at room temperature. Although enhanced light-exciton interactions in 2D TMDCs offer potential for novel photodetector devices, it is still unclear which mechanism governs the conversion of neutral excitons into free charge carriers for efficient photodetection. Hence, the aim of this thesis is to study the role of strongly bound excitons in photocurrent generation, and use external control of the exciton resonance to realise tuneable photodetection.

The structure of this thesis is as follows. In chapter 2, we provide a background on photodetection, 2D semiconductors and excitons. This is followed by a brief overview of state-of-the-art 2D photodetectors, and concluded by taking a closer look at WS_2 as a model system to study the influence of excitons on photocurrent generation. Subsequently, in chapter 3 we explain the process of fabricating 2D WS_2 photodetectors, followed by a description of our bespoke photocurrent spectroscopy and mapping setup in chapter 4. Thereafter, in chapter 5, we benchmark the setup with an existing Si nanowire array photodetector, fabricated by Li and co-workers at Stanford University [3]. Then, with everything in place, in chapter 6 the optical and optoelectronic properties of the fabricated 2D WS_2 photodetectors are characterised. Finally, in chapter 7 we summarise the main findings and provide an outlook for future research.

Chapter 2

Background

In this chapter, we start by addressing the principles of photodetection (2.1). Then, we introduce 2D materials and highlight a class of 2D semiconductors called transition metal dichalcogenides (2.2). Next, we explain the origin and consequences of excitons in (2D) semiconductors (2.3) and we highlight the variety of conceivable 2D photodetector device architectures with state-of-the-art examples from literature (2.4). Finally, we emphasise why WS_2 serves as a model system to study the role of excitons in photocurrent generation (2.5).

2.1 Photodetection

Photodetectors are semiconductor devices that can convert an optical signal into an electrical signal. The working principle of photodetection is based on the quantum photoelectric effect: a photon with sufficient energy can excite an electron from the valence band into an unoccupied state in the conduction band, creating an electron-hole pair [11]. The process is depicted with a schematic band diagram in Fig. 2.1(a). The energy ΔE associated with the optical transition is:

$$\Delta E = \frac{hc}{\lambda}\,, \tag{2.1}$$

where the right side of the equation is the photon energy E_ν, with Planck's constant h, speed of light c, and photon wavelength λ. The smallest transition energy is often simply the material's fundamental bandgap energy. However, in some cases optical transitions occur at sub-bandgap

energies due to, for instance, impurity or exciton states. In this case, the lowest-energy transition defines the semiconductor's optical bandgap.

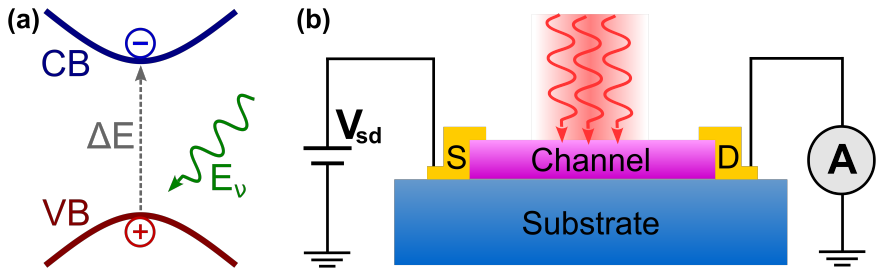

Figure 2.1: **(a)** Schematic band diagram showing the optical excitation of an electron (-) from the valence band (VB) into an unoccupied state in the conduction band (CB), leaving behind a hole (+). The transition energy ΔE is equal to the photon energy E_ν. **(b)** Schematic of a photodetector device on a substrate (blue). Charge carriers are photoexcited in the device channel (magenta). An external bias voltage (V_{sd}) is applied at the source (S) terminal, producing an electric field and separating the carriers. The photocurrent is extracted at the drain (D) terminal and measured by an Ampere meter (A).

In a photodetector, the photoexcited carriers are separated by an electric field and collected as photocurrent I_{pc}. The responsivity $\mathfrak{R}$ of the device can be calculated as:

$$\mathfrak{R} = I_{\mathrm{pc}}/P_{\mathrm{opt}}\,, \tag{2.2}$$

where P_{opt} is the incident optical power. A closely related metric is the external quantum efficiency, EQE, defined as the number of charge carriers produced per incident photon:

$$EQE = \frac{I_{\mathrm{pc}}/e}{\Phi_\nu}\,, \tag{2.3}$$

where e is the elementary charge and Φ_ν is the photon flux ($= P_{\mathrm{opt}}/E_\nu$). Ideally, the EQE should be unity, but in practice it is limited by losses due to charge recombination, incomplete absorption or reflection. Instead, the loss mechanisms are captured in the internal quantum efficiency, IQE, as:

$$IQE = \eta_{\mathrm{abs}} \cdot EQE\,, \tag{2.4}$$

where η_{abs} is the absorption efficiency of the detector. In contrast to the EQE, the IQE is difficult to assess experimentally. Though, if the IQE is wavelength-independent in the spectral range for which the detector is designed, the EQE becomes linearly dependent on

η_{abs}. Hence, if the illumination power and wavelength are known, the optical absorption of a photodetector can be probed by measuring the photocurrent.

Figure 2.1(b) schematically depicts a basic photodetector device architecture. Absorption of incident photons and creation of electron-hole pairs takes place in the device channel (magenta). An external bias voltage V_{sd} is applied at the source (S) terminal, producing an electric field to separate the electrons and holes. The carriers are extracted at the drain (D) terminal to provide the output signal, measured by the Ampere meter (A). Since a small current I_{dark} can flow in the device in the absence of illumination, the extracted photogenerated electrons and holes result in a net increase in current, the photocurrent. Hence, the total current measured by the Ampere meter is given by $I_{\text{sd}} = I_{\text{dark}} + I_{\text{pc}}$.

The described process is an example of photoconduction, i.e. the reduction of electrical resistance due to the extra charge carriers. Other relevant mechanisms influencing the extraction of photoexcited carriers are the photovoltaic effect and photogating. First, the photovoltaic effect describes the separation of charge carriers without any external bias, but instead by an internal electrical field originating from a p-n junction or a Schottky barrier. Second, photogating is the modulation of a detector's resistance by photogenerated carriers trapped in localised states. The electric field-effect of trapped holes (electrons) shifts the Fermi level, thereby increasing the electron (hole) density and effectively reducing (increasing) the resistance. Trap states are usually located at defects and surfaces, making this particularly important for devices with thin channels due to the large surface to volume ratio [1].

2.2 2D Semiconductors

2D materials are defined by their planar arrangement of atoms, with high crystalline order and no dangling bonds [1]. The atoms have strong in-plane covalent bonds, but the planes are held together by weak van der Waals interactions. This makes it possible to isolate single-unit-cell thick layers, known as monolayers, from a bulk crystal, forming natural quantum wells with high in-plane vs out-of-plane anisotropy. Only certain layered materials have been successfully isolated as air-stable 2D crystals. Nevertheless, there is a varied assortment of available 2D materials, from conductors (graphene) to insulators (hexagonal boron nitride, hBN) and semiconductors (transition metal dichalcogenides, TMDCs). A recent numerical assessment predicts a total of 1825 different 2D compounds that can be exfoliated, including

magnetic, topological, and half-metal systems [12].

One particular class of 2D materials - semiconducting TMDCs - have the chemical formula MX_2, where M is a transition metal and X a chalcogen. A single layer is 6-7 Å thick and consists of a hexagonally ordered plane of transition metal atoms sandwiched between two planes of hexagonally ordered chalcogen atoms [13], as shown in Fig 2.2(a). The layers exist in two distinct polytypes, depending on the relative orientations of metal and chalcogen atoms. TMDCs are primarily found in the trigonal prismatic (honeycomb) polytype, but for some TMDCs the thermodynamically stable phase is octahedral (centred-honeycomb) [14].

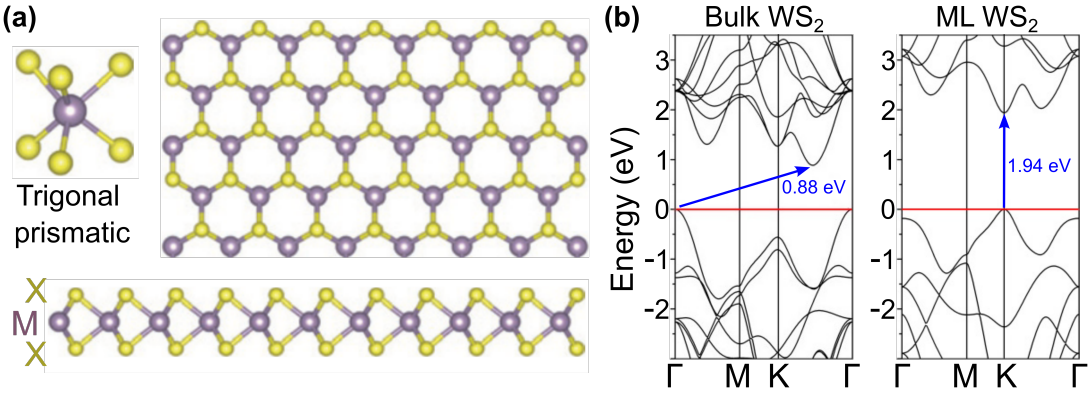

Figure 2.2: **(a)** Structure of a TMDC monolayer of the trigonal prismatic (honeycomb) polytype, adapted from [13]. **(b)** Density functional theory-calculated band structures of bulk and monolayer (ML) WS_2. The valence band maxima are indicated by the red lines and the fundamental bandgaps by the blue arrows, alongside the bandgap energies. The figure is adapted from [15].

The d-orbitals of group VIB transition metals, such as molybdenum (Mo) and tungsten (W), are half-filled. This leads to semiconducting behaviour with decreasing bandgap for increasing chalcogen atomic number. The band structure is dependent on the number of layers, as shown in the density functional theory-calculated band diagrams of bulk and monolayer WS_2, Fig. 2.2(b) [15]. TMDC monolayers have larger bandgaps than their bulk counterparts. Particularly, single layers of Mo- and W-based TMDCs have bandgaps with favourable energies in the near-infrared or the visible spectral range [16]. Moreover, when thinning TMDCs down from bulk to monolayer, they undergo a transition from an indirect bandgap at the Γ point in the Brillouin zone to a direct bandgap at the K point [15], as is visible in Fig. 2.2(b) for WS_2.

Transition metals are characterised by strong spin-orbit coupling and as a result the spin-degeneracy of the valence and conduction bands is lifted. Although the splitting is relatively small for the conduction band, the valence band separation reaches ~ 200 meV in Mo-based TMDCs and ~ 400 meV in W-based TMDCs. Hence, there are two distinct optical transitions from holes in the upper and lower energy spin valence bands [17].

2.3 Excitons

In a semiconductor, an electron-hole pair can be generated by absorption of a photon. The attractive Coulomb interaction between these oppositely charged particles can lead to the formation of a neutral, bound electron-hole pair called an exciton [6]. The energy of an exciton created in an optical transition is defined as:

$$E_{\mathrm{x}} = E_{\mathrm{g}} - E_{\mathrm{b}}\,, \tag{2.5}$$

where E_{g} is the bandgap energy and E_{b} is the exciton binding energy. Clearly, it is energetically favourable for excitons to be formed instead of free electron-hole pairs. Hence, we expect to observe strong optical absorption at energies below the fundamental bandgap. However, for bulk semiconductors, excitons are only observed in extremely pure samples, because impurities release unpaired electrons and holes in the material. Free charges screen the Coulomb attraction between the exciton's electron and hole and thereby strongly reduce E_{b}, which is on the order of ~ 5 meV in bulk materials [6]. Consequently, excitonic effects are practically absent in room-temperature optical spectra of conventional semiconductors, because the thermal energy, $k_B T \approx 25$ meV, is sufficient to dissociate the excitons into unbound carriers.

The study of excitons in quasi-2D systems such as GaN and GaAs quantum wells, with thickness on the order of ~ 10 nm, reveals that excitons in these systems are already more strongly bound, with $E_{\mathrm{b}} \approx 10$ meV [6]. In fact, the enhancement of E_{b} in these quantum wells is a consequence of one-dimensional quantum confinement of the electrons and holes. This forces the charge carriers closer together, thereby increasing the separation-dependent attractive Coulomb interaction. Accordingly, quantum well excitons show higher thermal stability than excitons found in bulk semiconductors.

In 2D TMDCs, the electron and hole that comprise the exciton experience almost ideal quantum confinement. In the monolayer limit, the electric field lines joining the electron

and hole start to protrude outside of the atomic plane, as shown in Fig. 2.3. As a result, the dielectric screening by the surrounding material is reduced and the binding energy is therefore enhanced even more [18]. Accordingly, in Mo- and W-based TMDCs, the binding energies can reach up to several hundreds of meV and are therefore stable at room temperature [17].

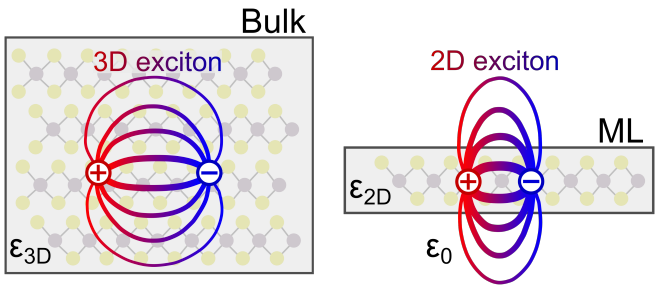

Figure 2.3: Real-space representation of excitons in bulk and monolayer (ML) TMDCs, with the change in dielectric environment indicated by the different dielectric constants in bulk (ε_{3D}) and in the monolayer (ε_{2D}), and the vacuum permittivity (ε_0). The figure is inspired by [18].

Besides the dielectric environment and charge confinement, the number of layers in a TMDC affects the excitons in other ways. For instance, inter-layer coupling causes additional optical transitions and carrier relaxation channels, thereby broadening the resonance features in optical spectra [19]. Yet, as the number of layers increases, E_x is only modestly (10-80 meV) redshifted, because additional layers cause a reduction in both E_b and in E_g. Furthermore, the exciton resonances are also influenced by charge doping, electrostatic gating, strain, impurities and defects, among others [17].

The exciton resonances in Mo- and W-based TMDCs can be separated into the spin-split A and B excitons. Here, A denotes the lowest-energy transition and therefore constitutes the optical bandgap. By carefully tuning the experimental parameters, the room-temperature absorption of monolayer TMDCs can reach up to $\sim 55\%$ at the A exciton resonance [20], despite being less than 1 nm thick. Moreover, since monolayers have a direct bandgap, radiative recombination of an exciton's electron and hole requires no phonon-assisted momentum transfer, resulting in drastically enhanced photoluminescence emission. In intrinsic monolayers, this amounts not only to emission from the A exciton, but also from other exciton-complexes such as charged excitons (trions) at room temperature and even biexcitons at cryogenic temperatures [21].

Since excitons are strongly bound neutral quasiparticles, they should in principle not contribute to the photocurrent. Though, as we will see in the next section, excitons certainly play a role in the generation of photocurrent by 2D TMDC photodetectors. Both theoretical [22] and experimental [23] works suggest that the strong electric fields may provide the energy necessary to overcome the large exciton binding energy, preventing recombination by splitting the excitons into free carriers. Regardless, the precise mechanism governing exciton dissociation remains unclear and requires further experimental investigation.

2.4 2D Photodetectors

Exciton-enhanced light-matter interaction combined with unique properties such as flexibility, gate-tuneability and high transparency make semiconducting TMDC nanolayers appealing candidates for future optoelectronic devices [9]. Moreover, the lack of dangling bonds on 2D material nanolayers frees the constraint of lattice matching [24], opening the doors for artificial heterostructures fabricated by stacking individual layers of different 2D materials. Countless heterostructures are conceivable due to the variety of available air-stable 2D materials and choice of substrate, stacking order and lateral orientation. In this section, we briefly explore various state-of-the-art 2D photodetectors.

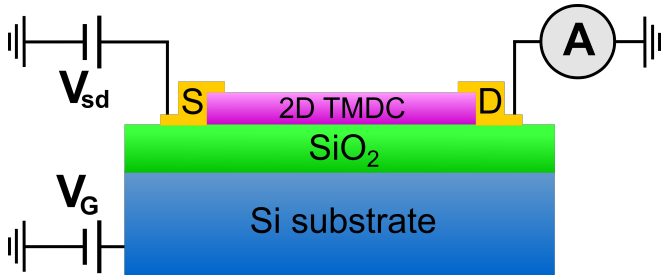

Figure 2.4: Schematic of a basic 2D TMDC FET architecture. The TMDC channel (magenta) is situated on an Si substrate (blue), where the thermal oxide layer (SiO_2, green) acts as gate dielectric. A bias voltage (V_{sd}) is applied at the source (S) electrode and measured by the Ampere meter (A) at the drain (D) electrode. Modulation is achieved with the back-gate (V_G).

Modulation of the optoelectronic properties of 2D photodetectors is commonly realised by electrical gating in a field-effect transistor (FET) architecture, depicted in Fig. 2.4. A FET-like device has not only source and drain terminals, but also a back-gate. An applied gate

voltage V_G shifts the conduction and valence bands, modulating the charge carrier density and thus the (photo)current. The minimum and maximum magnitudes of the current define the off- and on-state of the transistor, respectively.

High efficiencies and unique modulation potential have been demonstrated in multilayer WS_2 FETs. For instance, Lee and colleagues [25] achieve a responsivity of $\mathfrak{R} \approx 36$ A/W at the A exciton resonance by carefully tuning V_{sd} and V_G. Additionally, Yang *et al.* [26] have recently demonstrated an on/off current ratio of 8.5×10^7 and tuneable polarity behaviour from p-type at low V_{sd} through ambipolar to n-type at high V_{sd}.

Monolayer WS_2 photodetectors with graphene contacts are used by Wang and co-workers [27] to show absorption of sub-bandgap energy photons through upconversion. They report $\mathfrak{R} = 551$ mA/W at the A exciton resonance wavelength (620 nm), which defines the optical bandgap. Yet, upon increasing the wavelength to 680 nm, the responsivity reduces to $\mathfrak{R} = 59$ mA/W, which is unparalleled by conventional upconversion photodetectors.

In another work by Epstein and co-workers [20], monolayer WS_2 is encapsulated in hBN, which is very resistant to mechanical manipulation and chemical interactions while leaving the band structure of WS_2 nearly unperturbed. The heterostructure is gated by a gold back-reflector, forming an asymmetric Fabry-Pérot cavity with 55% excitonic absorption at room temperature, increasing to an astonishing 95% at 110 K. Moreover, they clearly demonstrate the ability to change between excitonic and trionic absorption by tuning V_G.

2.5 Tungsten disulphide

Although the potential of 2D TMDCs for photodetection applications is clearly demonstrated, the role of strongly bound excitons in photocurrent generation has not yet been fully elucidated. Here, we highlight why we use WS_2 to study the mechanisms of exciton dissociation.

First of all, the lowest-energy A exciton resonance is the most pronounced in monolayer WS_2, compared to other TMDCs [19]. Figure 2.5 shows the complex susceptibility $\chi = \varepsilon - 1$ of WS_2, with a remarkably strong oscillation in the magnitude (top) and a notable change in the phase angle (bottom) at the A exciton around $\lambda = 617$ nm. A gating-induced increase in electron density leads to screening of the electron-hole interaction and causes interconversion of excitons

to negatively charged trions [28]. Hereby, the excitons in WS_2 can be actively modulated and even reversibly quenched, causing one of the largest possible changes in material susceptibility.

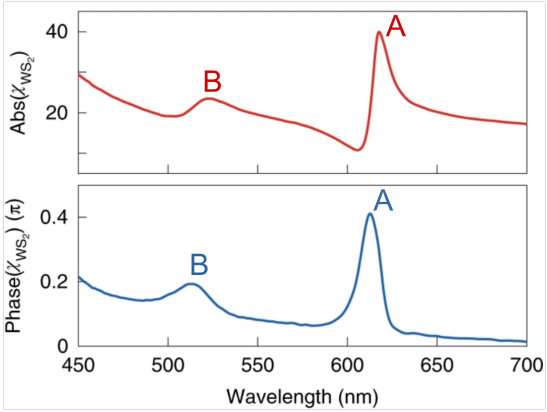

Figure 2.5: Susceptibility of WS_2, with the absolute value (top) and phase angle (bottom) of the material susceptibility. The B and A exciton resonances are indicated in the spectra. Adapted from [28].

Morover, the A exciton is well separated from the B exciton ($\lambda \approx 520$ nm), and both are found at favourable energies in the visible range. This is a result of the large spin-orbit splitting of the A and B excitons (0.38 eV [10]), and allows for a study of the A exciton unobscured by features from higher-energy excitons. Besides, the optical transitions in WS_2 exhibit narrow spectral features compared to other Mo- and W-based TMDCs [19], allowing for better quantitative comparison with theoretical predictions [18].

For this set of remarkable excitonic properties, WS_2 serves as a model system to study the role of strongly bound electron-hole pairs in photocurrent generation. Accordingly, in the next chapter we use mechanical exfoliation, deterministic transfer and lithography steps to fabricate 2D WS_2 photodetectors.

Chapter 3

2D WS_2 photodetector fabrication

In this chapter we describe the fabrication process of 2D WS_2 photodetectors. First, we explain how to obtain a single layer of WS_2 from a bulk crystal by mechanical exfoliation (3.1). Thereafter, we use computational techniques to provide a rationale for finding the optimal number of exfoliation steps to obtain monolayers (3.2). Next, we discuss how we identify monolayers by optical microscopy, Raman scattering and photoluminescence emission (3.3). Subsequently, we explain the deterministic transfer procedure of 2D WS_2 to a substrate (3.4). Finally, we tackle the fabrication of contact electrodes by which we turn 2D WS_2 into nanoscale photodetectors (3.5).

3.1 Mechanical exfoliation

The methods for obtaining monolayers can be subdivided into top-down and bottom-up approaches, i.e. the thinning of bulk crystals down to a single layer and the chemical growth of monolayers from its constituent atoms, respectively. Generally, top-down exoliation strategies produce the highest quality monolayers, but are unsuited for industrial upscaling. On the other hand, bottom-up approaches like chemical vapour deposition and epitaxial growth are promising for large-scale macroscopic production of 2D materials if reproducibility and quality issues can be overcome [29, 30].

While many avenues for the scalable production of high-quality large-area 2D materials are currently being explored, the 'Scotch-tape' mechanical exfoliation technique is the most accessible option to obtain high quality microscopic samples in the lab. The 'Scotch-tape' technique was first used for the isolation of graphene in 2004 [31] and other 2D materials in 2005 [7]. Since then, mechanical exfoliation has enabled the wide-spread exploration of the extraordinary properties of atomically thin materials. Although refinements to the original technique have been made, the general principles have remained largely unchanged. To start exfoliating, one needs some kind of adhesive tape, a substrate, and a piece of bulk layered material. In the following, we provide a comprehensive description of our protocol.

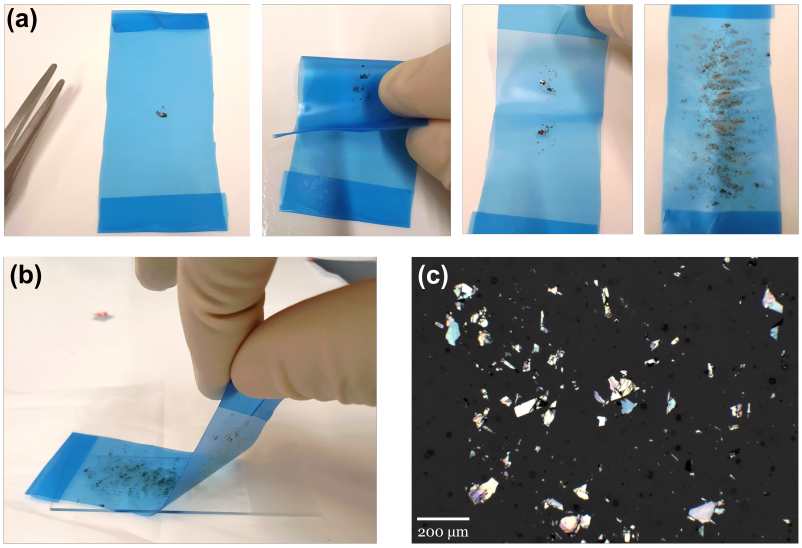

Figure 3.1: **(a)** Pictures of WS_2 exfoliation with Nitto tape. From left to right: A bulky flake is placed on the tape. The tape is folded, sticking it to the exposed WS_2 surface. Unfolding the tape cleaves the flake. Repeating the previous steps 4 to 8 times to obtain a large spread of thin WS_2. **(b)** Picture of the final exfoliation onto PDMS. **(c)** Optical microscope image of PDMS covered with many differently-sized WS_2 flakes.

We start with a bulk WS_2 crystal that is obtained commercially (HQ Graphene) and use Nitto SPV-224 tape for the exfoliation. To facilitate identification and transfer steps, described in sections 3.3 and 3.4, respectively, we use a $\sim 1 \times 1$ cm^2 rectangle of Gel-Pak WF-30 polydimethylsiloxane (PDMS) as substrate. The PDMS is placed on a glass microscope slide to

assist in exfoliation and identification. Besides, it allows for convenient storage in commonplace sample boxes, which we keep in a nitrogen desiccator.

The tape exfoliation procedure is depicted in Fig. 3.1(a). First, we place a small piece of bulk WS_2 on a strip of Nitto tape. We fold the tape and gently press it onto itself and the exposed WS_2 surface. Upon unfolding the tape, the WS_2 flake is cleaved into thinner flakes by exfoliation and laterally smaller ones by fracturing. The process is repeated around 4 to 8 times, depending on the bulk flake's initial thickness. In this way, we obtain many differently sized flakes spread out over a large portion of the tape. While it is important to repeat the process enough times to appropriately thin down the bulk flake, lateral fracturing of the flakes puts a limit on the number of repeated exfoliation steps before we end up with undesirably small flakes. This is discussed in detail in the following section.

After thinning down the bulk flake, we exfoliate one final time to the substrate, as shown in Fig. 3.1(b). The tape is gently pressed onto the PDMS, and a cotton tip is used to guarantee uniform adhesion, since air bubbles are sometimes trapped between the tape and PDMS. We release the tape in a swift motion, because in our experience this leaves the most flakes on the substrate. Placing the microscope slide with our sample under a 5x objective, we find the substrate covered with flakes of many different shapes and sizes, as shown in Fig. 3.1(c). We have no direct control over the shapes and sizes of the flakes. Thus, our method is geared towards high surface concentrations of flakes on the substrate, to improve the chances of obtaining suitable monolayers.

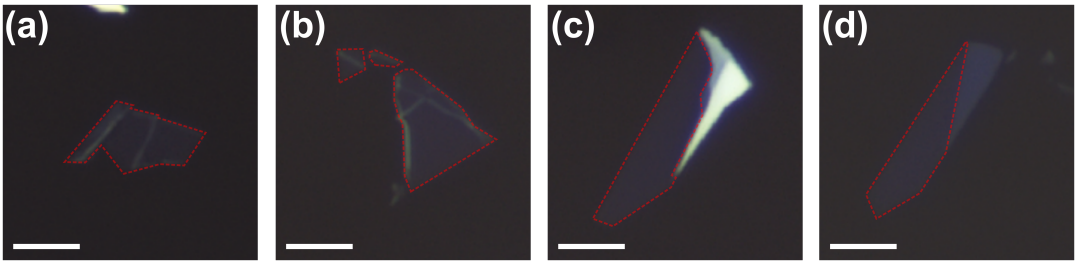

Figure 3.2: Optical microscope images of 2D WS_2 flakes on PDMS, with the monolayer areas outlined in red. Scale bars: 5 μm.

Some examples of atomically thin WS_2 obtained with the described procedure are shown in Fig. 3.2, with the monolayer areas outlined in red.

3.2 Computational estimation of the optimal number of exfoliations

As shown in the previous section, mechanical exfoliation is a somewhat crude procedure. Nevertheless, there exists a number of successive exfoliations that maximises the probability of obtaining a suitably-sized monolayer, as demonstrated by Ottaviano *et al.* [32]. Here we use a similar approach to stochastically model mechanical exfoliation and provide a rationale for obtaining the number of exfoliations that maximises the yield of monolayer flakes.

First, we consider mechanical exfoliation as a random uniform process. In other words, the cleaving can happen between any two layers with equal probability. The reasoning is that inter-layer van der Waals interactions are uniform across all interfaces. To avoid excessively hardware-intensive simulations, the serial exfoliation strategy proposed by Bohr is used [33]. This means that after every exfoliation one of two pieces is kept for further exfoliation and the other is discarded. Let $n(s)$ be the number of layers in a piece after s exfoliations. For any s, we set $1 \leq n(s) \leq n(s-1)$ with random uniform probability distribution. The flake peeling off the tape, i.e. $n(s) = 0$, is not allowed in the model. This is because the tape-flake interaction is very different and much stronger than the flake-flake interaction. We initialise the model by setting $n(0) = 1000$.

Second, we take into account lateral fragmentation of the flakes. Fragmentation during exfoliation is attributed to the lateral force component $F_{||}$ of the mechanical action [30]. $F_{||}$ creates a shear force, causing the flake to be laterally strained and thus introducing stress in the flake. We let $r(s)$ be the lateral size in μm after s exfoliations and the initial flake size $r(0) = 100\,\mu$m. We define the condition for fragmentation to occur at s as $n(s-1)/r(s-1) < 10$. The fragmentation condition is based on the intuition that a thick and laterally small flake is more likely to exfoliate, while a thin and laterally large flake is bound to fragment during exfoliation. The diffraction limit determines the minimum lateral size of a flake that can sensibly be located by optical identification. We take this into account by setting the minimal flake size at $0.5\,\mu$m. Hence, when the fragmentation condition is satisfied, the flake size is given by $0.5\,\mu\text{m} \leq r(s) \leq r(s-1) - 0.5\,\mu\text{m}$ with random uniform probability distribution. All in all, successive exfoliations yield not only thinner flakes, but also laterally smaller ones.

By simulating 10^7 independent serial exfoliations we computationally estimate the distribution

functions of $n(s)$ and $r(s)$ for 1 to 10 exfoliation steps. At $s = 1$ we find that the number of layers is uniformly distributed, but from $s \geq 2$ the probability of obtaining a monolayer, $P_{n=1}(s)$, is the highest. This makes sense, because a single layer at $s \geq 2$ can be obtained from any multilayered flake obtained at $s - 1$. After 8 exfoliations the model ends up with a monolayer more than half the time ($P_{n=1}(8) = 0.54$). However, the typical lateral size at $s = 8$ is below a few micron, which is too small for a practical photodetector device. Ideally, the flake's lateral size should be about 10 μm or larger to facilitate contact fabrication. The probability $P_{r>9}(s)$ of ending up with a flake that is large enough as a practical device vanishes as s increases.

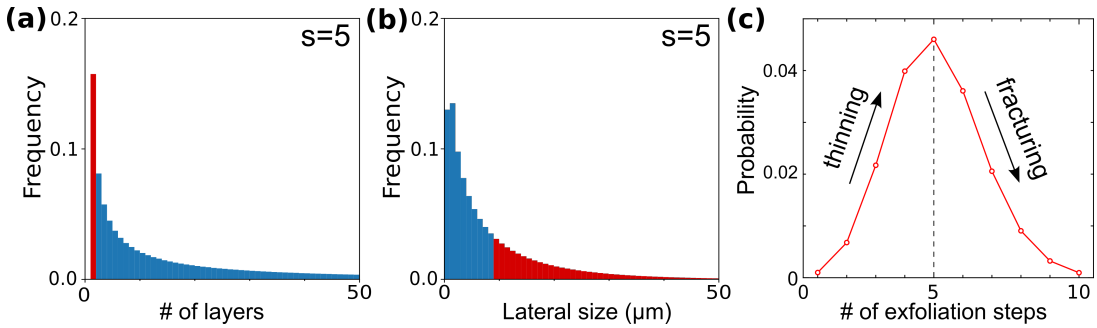

Figure 3.3: **(a)** The obtained probability distribution of the number of layers at $s = 5$. The frequency of obtaining a monolayer (0.16) is highlighted in red. **(b)** The obtained lateral size distribution at $s = 5$. The frequencies of obtaining a flake with $r > 9\,\mu$m (0.29 in total) are highlighted in red. **(c)** An estimation of the probabilities of obtaining a monolayer of $r > 9\,\mu$m for $1 \leq s \leq 10$. The optimal amount of exfoliations is $s = 5$, with a probability of 0.046.

Figure 3.3(c) shows the probability of obtaining a suitable monolayer flake after a certain number of exfoliation steps s, defined as $P_{\text{success}}(s) = P_{n=1}(s) \cdot P_{r>9}(s)$. We find that P_{success} increases rapidly for the first few exfoliatons and reaches a maximum at 5 exfoliations. Here, $P_{n=1}(5) = 0.16$ and $P_{r>9}(5) = 0.29$, giving $P_{\text{success}}(5) = 0.046$. The distribution functions for $s = 5$ are shown in Fig. 3.3(a) and (b), where the red-coloured bars indicate $P_{n=1}(5)$ and $P_{r>9}(5)$, respectively. We find that the probability of obtaining a monolayer rapidly decreases after the fifth exfoliation, and at ten exfoliations $P_{\text{success}}(10) < P_{\text{success}}(1)$. It is clear that the probabilistic sweet spot for obtaining a suitably-sized monolayer is small, and reached after only a few exfoliations. This trend is consistent with the results of Ottaviano *et al.* [32] and Bohr [33].

There are some caveats to the model, but these do not impact the general trend observed here. First of all, vertical exfoliation and lateral fragmentation are not (statistically) independent events. Therefore, simply multiplying $P_{n=1}(s)$ and $P_{r>9}(s)$ only gives a rough estimation of the actual $P_{\text{success}}(s)$ of obtaining a suitably sized monolayer. Generally, we expect that the practical probability is lower than the model value of $P_{\text{success}}(s)$, with the latter providing an upper bound for the procedure [30]. Besides, in the lab we need to transfer exfoliated flakes to a substrate, and we often encounter flakes with regions of different thicknesses. The model does not take these factors into account as they would severely complicate the model. The optimal amount of exfoliations is also dependent on the initial parameters chosen for the model and the quantisation of the fracturing criterion. However, the overall trend is robust for many different initial values and fracturing criteria. Thus, despite the limitations, the model gives valuable insight that provides a rationale for finding the optimal number of mechanical exfoliation steps. We have successfully implemented these insights in the lab, increasing the yield of suitably-sized WS_2 monolayers

3.3 Monolayer identification

Identifying WS_2 monolayers is accomplished by optical identification and confirmed by Raman and photoluminescence (PL) spectroscopy. For this, we use a WITec alpha300 confocal Raman microscope in the configuration that is schematically shown in Fig. 3.4.

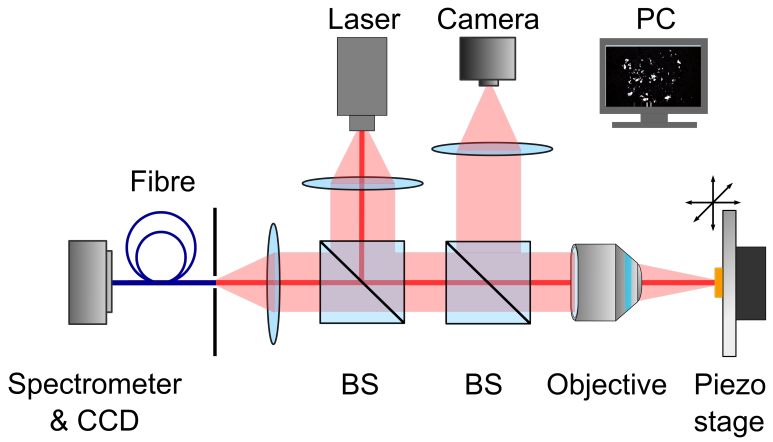

Figure 3.4: Schematic of the WITec microscope in confocal Raman configuration. The abbreviations CCD and BS are used for charge-coupled device and beam splitter, respectively.

The sample is mounted on a capacitively controlled piezo stage with 3 nm lateral positioning accuracy. For optical identification the sample is illuminated by a light emitting diode (LED). The reflected light is partially redirected to the camera by a beam splitter (BS), which can be moved in and out of the beampath. For Raman and PL spectroscopy a continuous wave laser with excitation wavelength $\lambda_{exc} = 532$ nm is moved into the beampath and focused to a diffraction-limited spot on the sample by a Zeiss EC Epiplan-Neofluar 100x objective (NA = 0.9). The scattered (Raman) or emitted (PL) light is collected by the same objective and detected with a fibre-coupled Witec UHTS 300 spectrometer (blaze wavelength 500 nm and 600 g/mm grating) and an Andor EMCCD. Most components of the microscope are controlled by the WITec Control software, allowing for straightforward acquisition of spectra and optical images.

In this section, we will first discuss how a trained eye can consistently identify 2D WS_2. After that, we will compare the bulk and monolayer Raman fingerprints. Finally, we will discuss room-temperature PL emission by a single layer of WS_2.

3.3.1 Optical identification

After the final exfoliation step onto a suitable substrate, one ends up with a large quantity of flakes spread out over a macroscopic area. The task of finding suitable flakes for the intended use is practically impossible with techniques such as atomic force microscopy (AFM) or scanning electron microscopy (SEM), due to the low throughput of these methods. Instead, the search for micrometer-sized few- and monolayer flakes relies on 'the high sensitivity, speed and processing power of the human eye and brain' [34].

Optical identification relies on differences in reflected light intensity between mono-, bi-, tri- (etc.) layers and bulk. This section aims to demonstrate that a trained eye can reliably distinguish flakes with different numbers of layers. First the red, green, and blue channel intensities of digital optical microscope images are analysed. After this, the optical contrast is calculated for mono- and few-layers to show that a distinction can indeed be made.

The reflected light intensity depends on the material and thickness of both the nanolayer and the substrate [35, 36]. A schematic of the reflection and refraction processes is shown in Fig. 3.5. Here, r and t are the reflection and transmission coefficients, n is the complex refractive index, and the subscripts 0, 1 and 2 denote air, nanolayer and substrate, respectively.

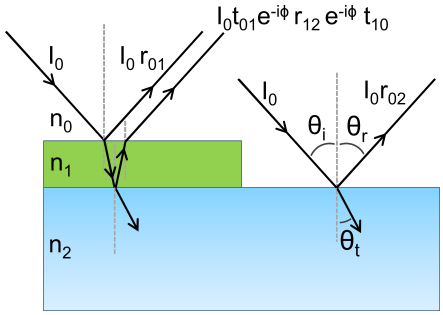

Figure 3.5: Schematic of reflection and refraction of a semi-infinite substrate (blue) and a TMDC nanolayer (green) on a semi-infinite substrate.

When a semi-infinite substrate is illuminated with light of intensity I_0 under normal incidence, the reflected light intensity is given by $I_{\text{sub}} = I_0 \left|r_{02}\right|^2$, where $r_{ij} = (n_i - n_j)/(n_i + n_j)$. If a 2D TMDC is placed on the substrate, new reflections and refractions must be considered. The intensity can then be calculated as:

$$I_{\text{2D}} = I_0 \left| \frac{r_{01} + r_{12}\, \mathrm{e}^{-2\Phi_1}}{1 + r_{01} r_{12}\, \mathrm{e}^{-2\Phi_1}} \right|^2 , \tag{3.1}$$

where $\Phi_1 = 2\pi n_1 d_1/\lambda$ is the phase shift and d_1 is the nanolayer's thickness. Since we always use PDMS as substrate, the number of layers is the only variable parameter in Eq. 3.1.

The difference in reflected intensities with varying TMDC thickness can be elucidated by optical microscope imaging. It cannot be ignored that the image displaying and capturing settings, e.g. brightness, contrast, saturation, etc., add many variables to the equation. Although in principle these can be held constant, in practice the settings are at least slightly different for every picture. Nevertheless, a meaningful analysis can be performed on flakes of different thicknesses captured in the same picture. For instance, the transmittance of mono-, bi-, and trilayer MoS_2 on PDMS have been correlated with the respective blue channel intensities by Hsu *et al.* [36].

Figure 3.6 depicts our investigation of the red, green, and blue channel intensities of WS_2 on PDMS captured in the optical microscope image of panel (a). The purple box indicates the region displayed in the colour maps of panel (c). These colour maps represent the 8-bit red, green and blue channels of the 24-bit optical image bitmap, i.e. for every pixel the three colours each have an intensity value ranging from 0 to 255. The dashed lines in the colour

maps represent the line traces plotted in the diagrams of panel (b), with the monolayer WS_2 regions indicated in the red colour map.

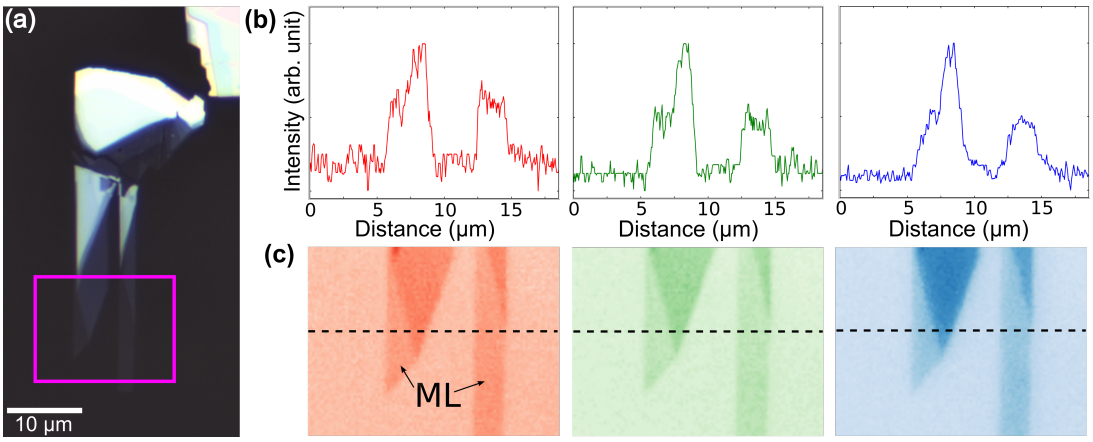

Figure 3.6: **(a)** Optical microscope image of WS_2 on PDMS. The purple box indicates the region displayed in the colour maps of (c). **(b)** From left to right: line traces of the red, green, and blue channel intensities. **(c)** From left to right: red, green and blue colour maps. The monolayer regions are indicated by 'ML' in the red colour map. The dashed lines indicate the line traces shown in (b).

We use 2D interpolation algorithms to go beyond the resolution of 57×57 nm^2 per pixel to an interpolated resolution of 1×1 nm^2 per pixel. The diagrams in (c) show the respective colour intensities obtained from line traces of the interpolated colour maps. There is an unmistakable step-wise difference in intensities of the substrate, mono-, and few-layer WS_2 for all three colours. We observe no notably improved contrast for any of the colours over the others, as reported by Hsu *et al.* [36] for blue channel images of MoS_2 on PDMS. Regardless, we find a significant difference in contrast between mono- and few-layer WS_2 flakes.

To further investigate this, we use the total intensities I_{sub} and I_{2D} of the substrate and WS_2, respectively, to calculate the Michelson contrast [32]:

$$\text{Contrast} = \frac{I_{\text{sub}} - I_{\text{2D}}}{I_{\text{sub}} + I_{\text{2D}}} \,. \tag{3.2}$$

Using this formula, changes and fluctuations in imaging conditions are divided out. Moreover, local variations in intensity are averaged out by taking the mean intensity of 625 (25×25) pixels. This is demonstrated in Fig. 3.7(a), where the squares indicate the regions over which

the intensity is averaged for monolayer WS_2 (red), PDMS substrate (blue), and few-layer WS_2 (green).

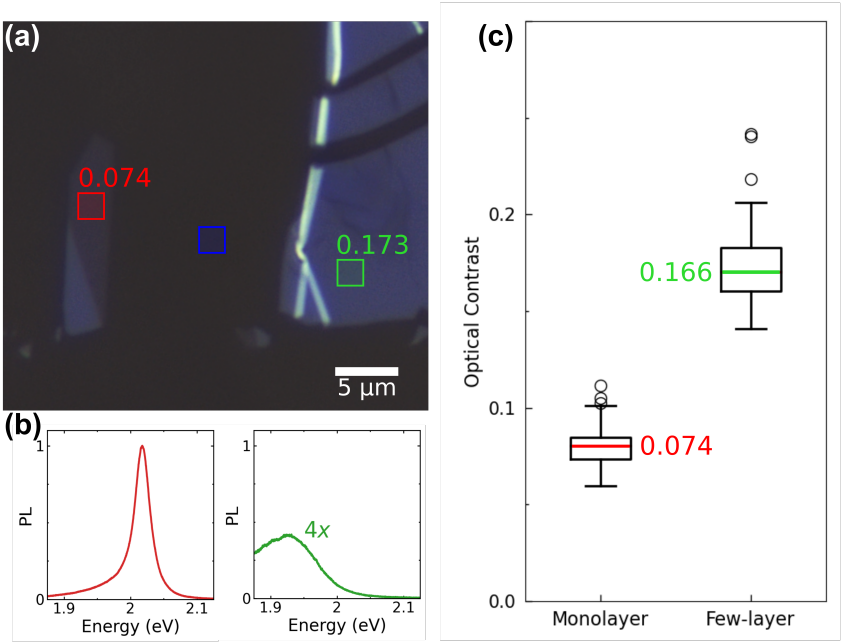

Figure 3.7: **(a)** Optical image of mono- and few-layer WS_2 flakes on PDMS. The boxes represent the integrated area of few-layer (green), substrate (blue), and monolayer (red) respectively. **(b)** Left: Representative PL spectrum of monolayer WS_2. Right: Typical PL spectrum of few-layer WS_2, with the intensity multiplied by 4 for visibility. **(c)** Boxplot of the Michelson contrast for 34 mono- and 37 few-layer WS_2 flakes. The coloured lines indicate the median values, the boxes indicate the IQR, the whiskers indicate non-outlier data ($1.5 \cdot \text{IQR}$), and the circles represent outliers.

We use photoluminescence (PL) spectroscopy to verify that a flake is indeed monolayer or few-layer. Representative spectra of monolayer (red) and few-layer (green) WS_2 are shown in Fig. 3.7(b). We define a monolayer as having an intense and narrow PL peak and a few-layer as having a small, broad, but non-negligible PL signal. PL spectroscopy is more thoroughly explained in section 3.3.2.

The optical contrast is calculated for 34 different monolayers and 37 few-layers, and the result is plotted in Fig. 3.7(c). The median value of the monolayer contrast (red) is 0.074, whereas the median value for few-layers (green) is 0.166. The boxes around the medians indicate

the interquartile range (IQR), the whiskers are set to 1.5 times the IQR. The circles show outlier values, i.e. values beyond $1.5 \cdot \text{IQR}$. There is a clear distinction between the contrast of mono- and few-layer WS_2 on PDMS. Moreover, there is no overlap between the optical contrasts. Thus, in principle, measuring the optical contrast of a WS_2 nanolayer on PDMS and comparing it to the presented data is sufficient to determine whether it is a monolayer or not, with Raman and PL spectroscopy as final methods for verification.

3.3.2 Raman spectroscopy

Raman scattering is a form of inelastic light scattering from phonons subdivided into Stokes and anti-Stokes scattering, or excitation and annihilation of a vibrational quantum, respectively [6]. Due to conservation of momentum and energy, light is redshifted compared to elastic scattering in a Stokes scattering event and blueshifted in an anti-Stokes scattering event. Raman modes originate from these frequency shifts, which are characteristic for a material and therefore the Raman spectrum provides a fingerprint of the material involved.

Raman scattering of few- and monolayer of 2D TMDCs can be used to determine the number of layers. The Raman responses of mono-, bi-, trilayer and bulk WS_2 for different excitation wavelengths are reported in literature [37–39] and serve as a well-established reference. The typical Raman spectrum of WS_2 is dominated by first-order optical modes at the Brillouin zone centre, $E^1_{2g}(\Gamma)$ (in-plane) and $A_{1g}(\Gamma)$ (out-of-plane), and longitudinal acoustic mode LA(M) at the zone edge [38]. The Raman shift $\tilde{\nu}$ of the modes is dependent on the excitation wavelength λ_{exc} as

$$\tilde{\nu} = \left(\frac{1}{\lambda_{\text{exc}}} - \frac{1}{\lambda_{\text{scat}}} \right) , \tag{3.3}$$

where λ_{scat} is the wavelength of the scattered light. For a WS_2 flake with many layers and $\lambda_{\text{exc}} = 532$ nm, we find 2LA(M) at 351 cm^{-1}, $E^1_{2g}(\Gamma)$ at 356 cm^{-1} and $A_{1g}(\Gamma)$ at 420.5 cm^{-1}, as shown in the green spectrum in Fig. 3.8(a). The 2LA(M) mode overlaps with the $E^1_{2g}(\Gamma)$ mode, increasing the uncertainty in determining the respective Raman shifts. This effect is stronger for the monolayer, as the two peaks appear slightly more separated in the bulk spectrum.

The monolayer Raman spectrum is shown in red in Fig. 3.8(a). One can immediately notice the decreased peak intensity of the three discussed modes. The relative intensities of the combined $2LA(M)/E^1_{2g}(\Gamma)$ peak compared to the $A_{1g}(\Gamma)$ peak drastically change when going to the monolayer limit, with a stronger decrease in intensity of the $A_{1g}(\Gamma)$ mode. This is attributed

to a decreased phonon restoring force, caused by van der Waals interactions between layers in multilayer WS_2 [38]. Moreover, we observe a redshift of the $A_{1g}(\Gamma)$ peak frequency to approximately 418 cm^{-1}, consistent with reports in literature [38, 39], and also attributed to the suppression of inter-layer phonon restoring forces. We do not observe the blueshift of the $E^1_{2g}(\Gamma)$ mode reported by Qiao *et al.* [39]. This may be due to the overlap of this mode with the 2LA(M) mode, complicating the analysis of either mode. Nevertheless, the observation that the $A_{1g}(\Gamma)$ peak amplitude reduces almost to the background level is consistent across all measurements we performed on monolayer samples. In contrast, the amplitude of the $A_{1g}(\Gamma)$ peak of bulk WS_2 is considerably larger than the background level. Although it is not shown here, this trend holds even for bi- and trilayer WS_2 [38]. For this reason, we can quickly distinguish monolayer from multilayer WS_2 by means of Raman spectroscopy.

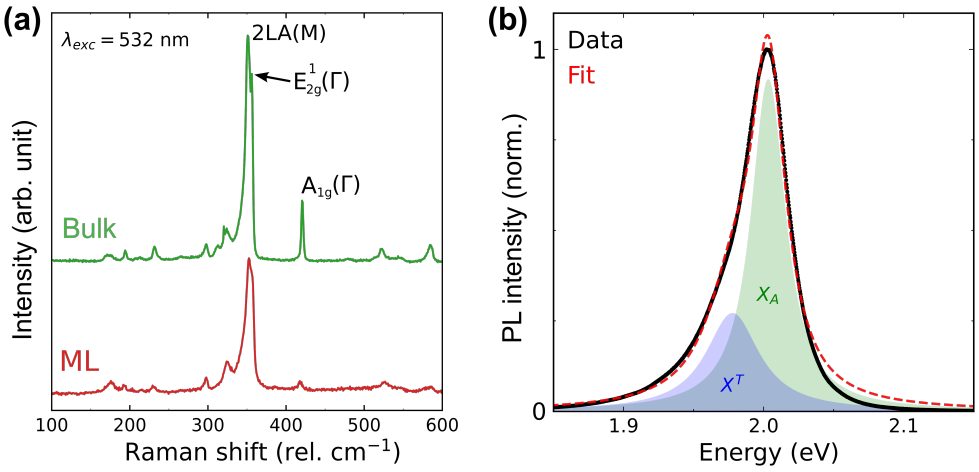

Figure 3.8: **(a)** Representative Raman spectra of bulk (green) and monolayer (red) WS_2 for $\lambda_{exc} = 532$ nm. The spectral positions of the most relevant phonon modes are indicated for the bulk spectrum. **(b)** Representative PL spectrum of monolayer WS_2 on PDMS. The black datapoints indicate the measured data, the red dashed line indicates the double Lorentzian fit, the green area indicates the contribution from the A-exciton at 2.00 eV with FWHM of 14.9 meV, and the blue area indicates the contribution from the trion at 1.98 eV with FWHM of 23 meV.

3.3.3 Photoluminescence spectroscopy

Photoluminescence (PL) spectroscopy is the most convincing method for the identification of WS_2 monolayers with the WITec confocal microscope setup. Greatly enhanced PL emission is observed for monolayers compared to bulk, related to the indirect-to-direct bandgap transition [40]. Room temperature PL measurements are usually preferred, because contributions from defect states become more pronounced at cryogenic temperatures [9].

The room temperature PL spectrum of monolayer WS_2 on PDMS is dominated by the combined A exciton and trion peak around 2 eV, as shown in Fig. 3.8(b). The PL is normalised and fitted by a double Lorentzian to disentangle the contributions of the A exciton (X_A) and the negative trion (X^T). We find that A exciton emission peaks at $2.00 \pm 9.6 \cdot 10^{-5}$ eV, with a spectral width (defined by the full width at half maximum, FWHM) of 14.9 ± 0.2 meV. For the trion we find the peak emission at $1.98 \pm 6.2 \cdot 10^{-4}$ eV and a spectral width of 23.0 ± 0.5 meV. These results are in good agreement with exciton and trion energies and their PL linewidths reported in literature [41–46].

In contrast to the monolayer limit, PL emission from few-layer WS_2 is characterised by a small, broad, and red-shifted PL peak compared to monolayer PL, as seen in Fig. 3.7(b) in the previous section. This is attributed to increased screening of the exciton, decreased quasiparticle bandgap energy, and the transition to an indirect bandgap [18]. The quantitative difference in PL intensities of monolayers and multilayers measured under the same conditions varies wildly, and we observe monolayer PL intensities anywhere from 10 to 200 times as strong as few-layer PL intensities. One reason is that we do not determine the number of layers in the few-layer samples, because we are particularly interested in monolayers. However, the few-layer PL intensity is dependent on the exact number of layers, with decreasing PL intensity as the number of layers increases [9]. Moreover, factors such as sample quality and strain affect the PL intensities of WS_2 nanolayers, complicating a rigorous quantitative comparison. However, qualitatively, the room temperature PL emission from WS_2 with more than one layer is negligible compared to monolayer PL emission. Hence, PL spectroscopy provides convincing proof that a WS_2 nanolayer is indeed a monolayer.

3.4 Deterministic transfer

The stochastic nature of mechanical exfoliation prevents direct, reliable placement onto a substrate. Fortunately, various deterministic transfer techniques have been developed for the accurate placement of 2D materials, enabling top-down assembly of devices and heterostructures. Accordingly, the development of accurate transfer methods for 2D materials is regarded as one of the most important breakthroughs in 2D materials research [47].

In the following, we first explain the the all-dry deterministic transfer technique proposed by Castellanos-Gomez and colleagues [47, 48]. After that, we provide a detailed description of the experimental stamping setup and the procedure of transferring WS_2 nanolayers onto a patterned SiO_2/Si substrate. We end this section with several remarks on the process.

The technique developed by Castellanos-Gomez *et al.* [48] makes use of viscoelastic stamps. In contrast to many other transfer techniques, the process is all-dry, i.e. no wet chemical process is required. This widens the range of applications and avoids contamination of the fabricated structures. Furthermore, flakes can be exfoliated directly from Nitto tape onto the stamp. This streamlines the entire device fabrication process, because when a suitable flake is identified, it is promptly mounted to the stamping stage. If, however, the exfoliation is unsuccessful, the stamp is simply discarded.

The technique's working principle is based on viscoelasticity: on short time scales the stamp behaves like an elastic solid, while on longer timescales it behaves as a viscous fluid. As a result, slowly peeling the stamp detaches it from the flakes, which preferentially adhere to the substrate [48].

The stamping setup is shown schematically in Fig. 3.9(a) and an optical image of the setup is provided in Fig. 3.9(b). For the transfer procedure, we use the WITec microscope described in section 3.3.2, with Zeiss Epiplan 5x, 20x, and 50x long working distance (LWD) objectives in bright-field mode. As substrate, we use silicon (Si) with a 100 nm thick layer of thermal oxide (silica, SiO_2), and a rectangular grid of 30 nm thick gold (Au) alignment markers. The substrate is mounted to the sample stage with Scotch Sticky Tab double-sided tape. The sample stage has XY micromanipulators for manual adjustments of the substrate, an XYZ piezo stage for computer-controlled sub-micron alignment, and a custom rotation mount, denoted by θ, to manually adjust the azimuthal orientation of the substrate. The stamp consists of Gel-Pak

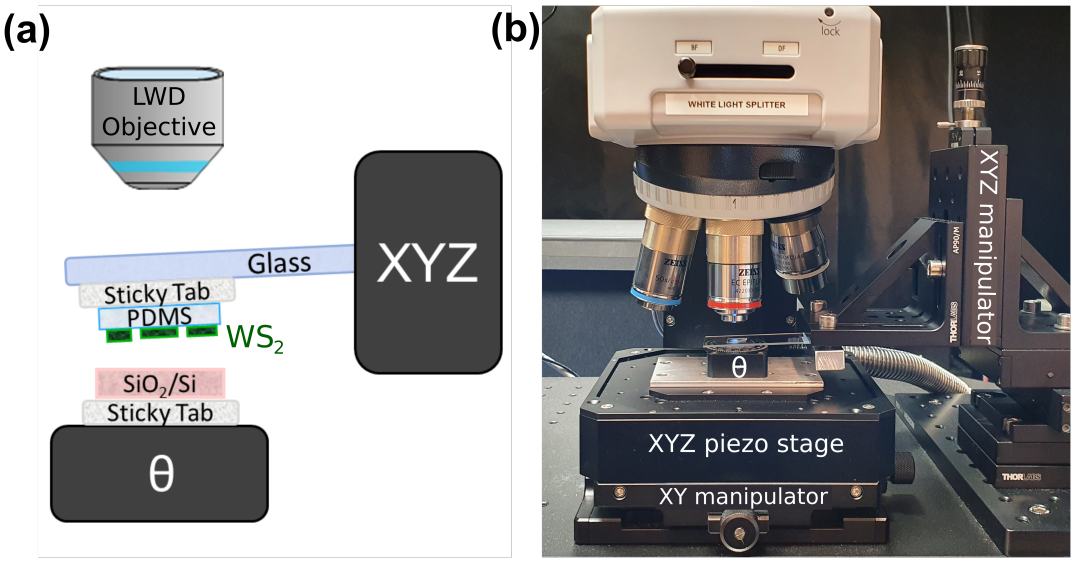

Figure 3.9: **(a)** Schematic of the stamping setup, with the following short-hand notations. LWD: long working distance, θ: rotation stage, XYZ: XYZ manipulator. **(b)** Picture of the stamping setup, with components labelled in white.

WF-30 PDMS as viscoelastic material, attached to a glass microscope slide with a Sticky Tab.

All the stamp materials are transparent, allowing us to look through the stamp and focus on the 2D material and the substrate with LWD objectives. The glass slide is mounted onto an XYZ manipulator, which allows us to position the stamp with sub-micron precision. The slide is held at a slight (polar) angle to ensure that the stamp comes into contact with the substrate gradually for a controlled stamping procedure.

Figure 3.10 shows the stamping procedure as viewed with the 5x objective. First, we focus on the desired part of the substrate and align it correspondingly (a). The gold crosses, visible in each of the four corners, allow us to determine the exact coordinates of the nanolayers after stamping, as explained in the following section. Then, we mount the stamp onto the XYZ manipulator and position it over the substrate. We can focus on the flakes or look through the stamp and focus on the substrate, as shown in panels (b) and (c), respectively. After we are satisfied with the position and orientation of the stamp with respect to the substrate, we lower the stamp so that it starts to come into contact with the substrate. Because the stamp

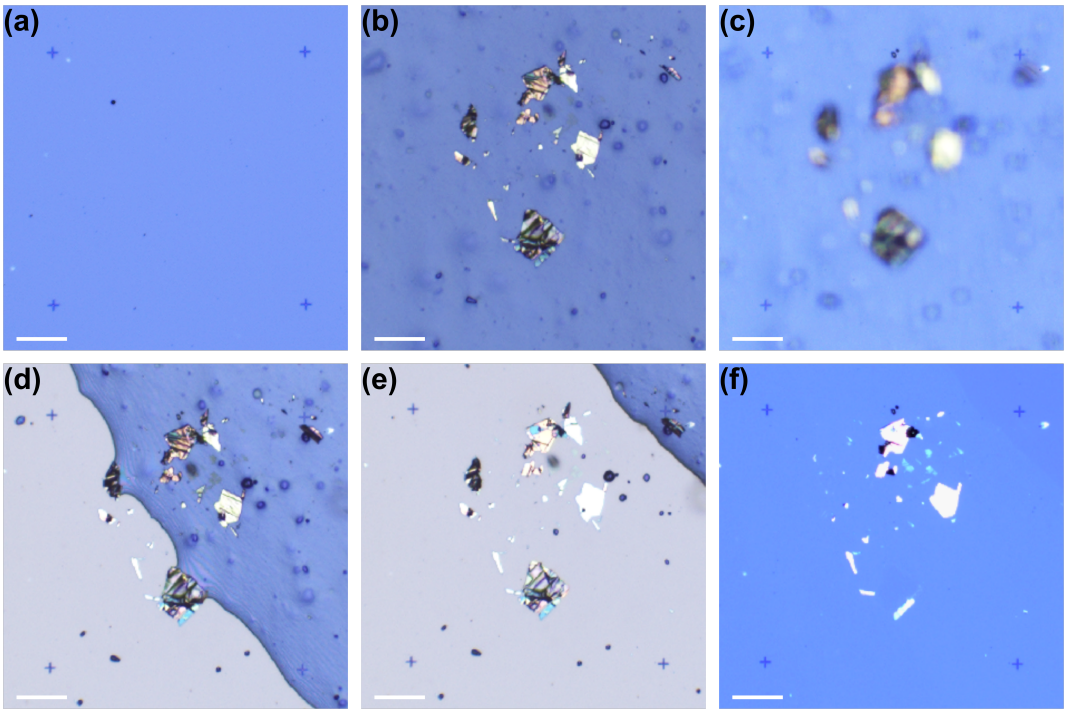

Figure 3.10: Optical microscope images of the deterministic transfer procedure. Scale bars: 100 μm. **(a)** Target area on the substrate, demarcated by Au markers in each of the four corners. **(b)** WS_2 flakes on the viscoelastic stamp. **(c)** Focusing on the substrate through the stamp. **(d)** The stamp and substrate start to come into contact. The contact region appears grey, while the uncontacted region appears blue. **(e)** After lowering the stamp even further, the entire region of interest is in contact. **(f)** The WS_2 flakes are transferred to the substrate.

is mounted at a slight angle, the stamp and substrate first come into contact in the lower left. When the stamp is further lowered, air is pushed out to the upper right. This gives the illusion of a travelling wave front, as shown in panels (d) and (e), which is an indicator of successful contact. When the entire region of interest is in contact we slowly raise the stamp again until it is completely detached from the substrate, leaving behind the WS_2 flakes (f). Figure 3.11 shows images of three candidate photodetectors taken using the 100x objective.

The success rate we achieve with the described technique is low, thus it is worth pointing out some issues often encountered and what might be done to improve the repeatability. First

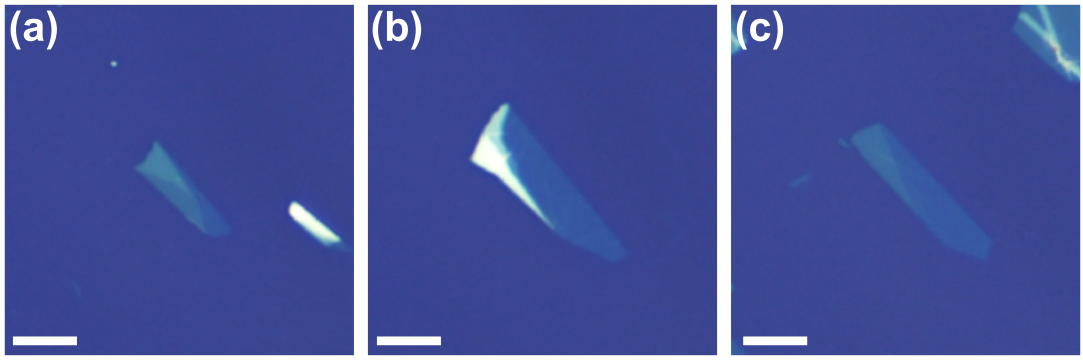

Figure 3.11: Three optical microscope images of candidate WS_2 flakes deterministically transferred to the Si/SiO_2 substrate. Scale bars: 5 μm.

of all, there is the need to attach the PDMS to the glass slide. Although PDMS sticks to glass, the adhesion is weak, which sometimes causes the PDMS to come off during transfer and remain stuck to the substrate. Cleaning the glass slide with ethanol and blow-drying it with nitrogen improves the adhesion, but does not completely solve the problem. Hence, we use a Sticky Tab as a transparent adhesive. Unfortunately, Sticky Tabs are quite thick ($\sim$1-2 mm), causing diminished contrast and focus, especially with higher magnification objectives.

In this regard, the technique described by Zhao *et al.* [47] looks promising. The authors do not peel the PDMS from its transparent back-cover, instead they place the PDMS attached to the back-cover hanging over the edge of the glass slide, securing it with Scotch tape. By itself, PDMS is too flexible for this geometry, but the back-cover acts as a transparent support structure. The contrast and focus are enhanced compared to the technique we use, since the back-cover is only 0.2 mm thick. However, in our experience, the caveat is that exfoliation onto the stamp and subsequent mounting to the stamping stage is cumbersome and more time-consuming. Nevertheless, if this issue is overcome, it could prove to be an excellent deterministic transfer technique.

3.5 Contact fabrication

Now that WS_2 nanolayers are successfully transfered to the substrate, they can be turned into actual photodetector devices. The first step towards this end is calculating the exact substrate

coordinates of the candidate photodetectors. After that, nanoscale contact electrodes are lithographically fabricated. Finally, the substrate with devices is mounted on a custom sample holder and wire bonded to it.

3.5.1 Coordinate calculation

To facilitate the lithographic electrode fabrication, we need to know the precise coordinates of each of the candidate photodetectors on the substrate. To this end, there are four large (200×200 μm) alignment markers situated in each of the substrate's four corners and a 10×10 rectangular grid of small (20×20 μm) markers spaced 480 μm or 500 μm apart. We use a Zeiss Epiplan 20x objective to take pictures of the flakes, because with this objective the image dimensions are approximately 560 μm by 350 μm, allowing us to have two small markers in the field of view simultaneously. Since we know the separation and orientation of the markers, we can accurately determine the image's resolution (0.284×0.284 μm^2/pixel) and rotation angle of the substrate and use these to calculate the absolute positions of flakes.

We code a Python program to calculate the coordinates from optical microscope images of the flakes and alignment markers. In the program, we first zoom in and click on two small markers to define the coordinate system. Then, we click on each of the corners of the WS_2 flake to define a polygon representing it. The program uses the coordinate system to determine the positions of the polygon's vertices. Finally, the program saves a text file with each of the vertices' coordinates, as well as an image file of the polygon overlaid on the microscope picture, with each of its vertices labelled.

The accuracy of the calculated coordinates is mostly limited by the need to manually click on each of the vertices. Still, we can repeatedly pinpoint a vertex within $\leq$0.81 μm (2.85 pixels), as determined by recalculating the vertex's coordinates ten times. We take this as the precision limit of the coordinate calculation procedure.

3.5.2 Electron-beam lithography

Electron-beam (e-beam) lithography is a flexible technique for producing nanostructures on a substrate. First, we use the KLayout software to design the large and small alignment markers and fabricate these using the procedure described below. As mentioned, these markers allow

us to determine the positions of the transferred WS_2 flakes on the substrate. We load the coordinates into KLayout to design the contact electrodes, tailored to each of the six candidate WS_2 devices. Figure 3.12 shows the designs of three devices within the same write field, which is determined by the alignment markers (visible in each of the four corners). All the device designs consist of source and drain electrodes, with each electrode consisting of a 1 μm wide L-shaped channel connected to 5 μm wide contact leading to a 250×250 μm^2 contact pad.

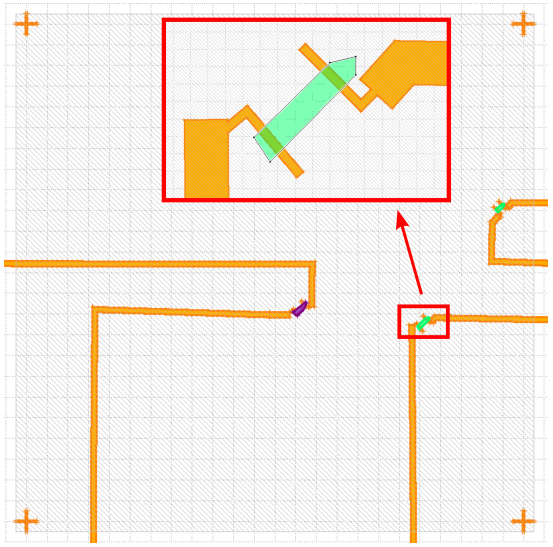

Figure 3.12: Screen capture of the KLayout software, showing the designs of three 2D WS_2 photodetectors in a single write field, demarcated by the alignment markers in each of the four corners. The polygons represent the few-layer (green) and monolayer (purple) WS_2 channels, with the designed gold contacts (orange). Each square in the grid represents 20×20 μm^2. The inset shows a close-up of one of the devices ("IJ").

The lithographic procedure is shown in figure 3.13(a). First, we spin-coat a thin layer of positive-tone E-Beam Resist AR-P 6200.09 (CSAR 62) on the substrate (1). Then, we write the desired structure in the resist with an electron-beam (2) and selectively remove the resist in development step (3), to create a mask for the final metal structure. We apply the first developer, n-amyl acetate, for 60 seconds to get sharp edges and the second developer, o-xylene, for 5-7 seconds to remove any remaining particles from the first developer. We stop the development with a mixture of methyl isobutyl ketone (MIBK) and isopropyl alcohol (IPA) in a 9:1 ratio. After development, the substrate with WS_2 flakes and developed mask layer

clearly show the lithography pattern, Fig. 3.13(b).

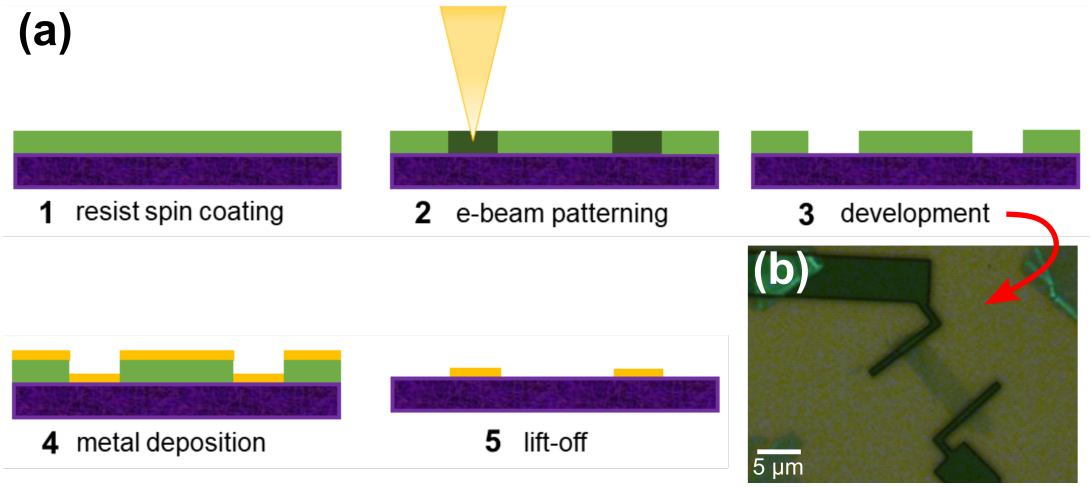

Figure 3.13: **(a)** Schematic of the e-beam lithography process. **(b)** Optical microscope image taken after development. The WS_2 flake and the substrate are covered with e-beam resist, except for the regions of the designed contacts, where the resist is removed by e-beam patterning.

Subsequently, we deposit a thin adhesion layer and a layer of metal on the entire surface (4), 3 nm germanium with 30 nm gold for the markers and 3 nm chromium with 100 nm gold for the contacts. We remove the resist and excess metal in the lift-off step (5) by submerging the sample in 70 °C anisole until all resist is gone, leaving only the designed structure. Finally, we clean the substrate with acetone and IPA, and dry it by blowing nitrogen over the top.

Unfortunately, only two of six candidate flakes were still present on the substrate after the lithographic procedure, and it is unclear in which step the other four flakes got removed from the substrate. Figure 3.14 shows the fabricated contacts, with the WS_2 flake missing in (a), and the successfully contacted flakes making up devices "GH" (b) and "IJ" (c), with the full electrode architecture shown in (d). The letters G, H, I and J refer to the contact pads of the sample holder, to which each of the microscale contacts will be wire bonded in the next section.

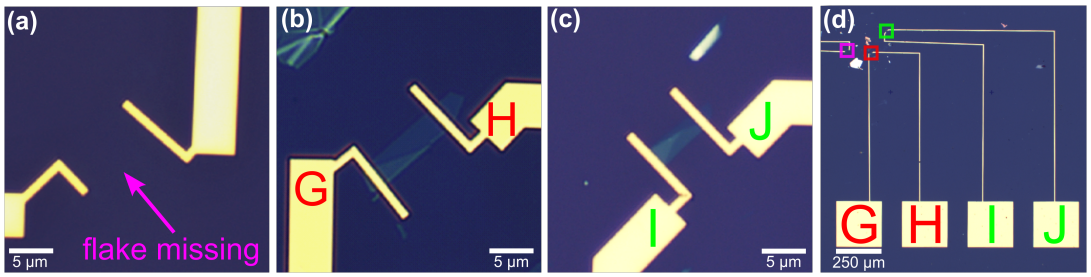

Figure 3.14: Optical microscope images of 2D WS_2 photodetectors with gold contacts on a Si/SiO_2 substrate. **(a)** The WS_2 flake is missing. **(b)** Device "GH" **(c)** Device "IJ" **(d)** Optical microscope image showcasing the device architectures of devices "GH" (red) and "IJ" (green), with the area of the missing flake also highlighted (magenta).

3.5.3 Wire bonding

After completion of the nanoscale Au electrodes and contact pads, we attach the patterned substrate to a custom-made sample holder with double-sided tape, making sure not to touch any of the sample holder's Au contacts pads. Next, we use a West·Bond 7KE wire bonder to manually interconnect the contact pads of the devices and the sample holder. The wire bonder is equipped with an Olympus Model SZ51-60 stereo microscope with 0.8-4× magnification and has an XYZ micromanipulator that is directly linked to the 45° wedge bonding head assembly. With the tool, we manually bond 25 μm Al wires to the contact pads of the devices and sample holder by applying ultrasonic power for tens to hundreds of milliseconds.

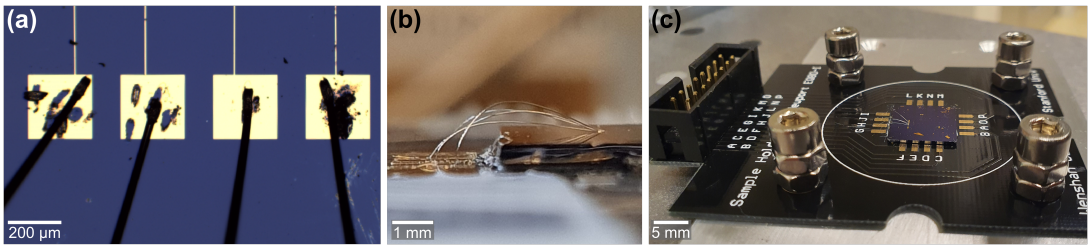

Figure 3.15: **(a)** Optical microscope image of the contact pads after wire bonding, with clearly visible residue from the failed bonding attempts. **(b)** Side-view of the wire bonds connecting the source and drain contacts of the devices to the sample holder. **(c)** Picture of the substrate with WS_2 photodetectors wire bonded to the sample holder, which is secured to the custom mount for the WITec microscope.

We have at least one failed attempt at bonding each of the four bonds (two per device), which is generally undesirable. Figure 3.15(a) shows a microscope image of the bonds to the contact pads, with multiple holes in the contact pads clearly visible. We attribute the failed attempts to using the wrong wire bonder settings, which were optimised for bonding to an aluminium foil practice surface, which has a much higher surface roughness than the gold deposited in the lithography step. The settings should be optimised for the smoother gold surface to avoid needing multiple bonding attempts.

Nevertheless, the devices' source and drain contacts are now connected to the sample holder, as shown in Fig. 3.15(b), and the holder is secured to a custom mount for the WITec's sample stage to warrant highly stable sample mounting in the microscope, see Fig. 3.15(c). The two photodetector devices are now ready for testing and characterisation, which will be discussed in chapter 6.

Chapter 4

Photocurrent mapping and spectroscopy setup

In this chapter, we describe and benchmark our home-built photocurrent mapping and spectroscopy setup, which provides full control over the polarisation, wavelength and power of the excitation laser. The setup is integrated with the WITec microscope to take advantage of the WITec's piezo stage for scanning photocurrent microscopy and sample positioning with ~ 3 nm precision. Additionally, the setup allows for simultaneous reflection measurements, to correlate the photocurrent data with the exact position on the sample.

We start by describing the experimental setup (4.1), starting with the electronics, followed by the optics and concluded by a brief description of the computer-controlled experiment automation. Subsequently, we describe various benchmarking steps (4.2), starting with the current-voltage characteristic of the sample holder, the laser power spectrum, and the laser stability over time. After that, we discuss the polarisation optics and calibration thereof. Finally, we determine the radial resolution and depth of focus by performing a knife-edge measurement in the reflection geometry.

4.1 Experimental setup

The experimental photocurrent mapping and spectroscopy setup, schematically depicted in Fig. 4.1, involves electronics (red), a free-space laser setup (green), the WITec microscope (blue) and a separate detector for reflected light, all integrated and automated with Python on the lab computer (PC).

First, we describe the electronics and highlight the merits of lock-in detection. Afterwards, we give a rundown of the optical elements for the free-space excitation laser beam path and the fibre-coupled detector. The WITec microscope is described in section 3.3 and therefore not discussed here. Finally, we provide a brief description of the experiment automation.

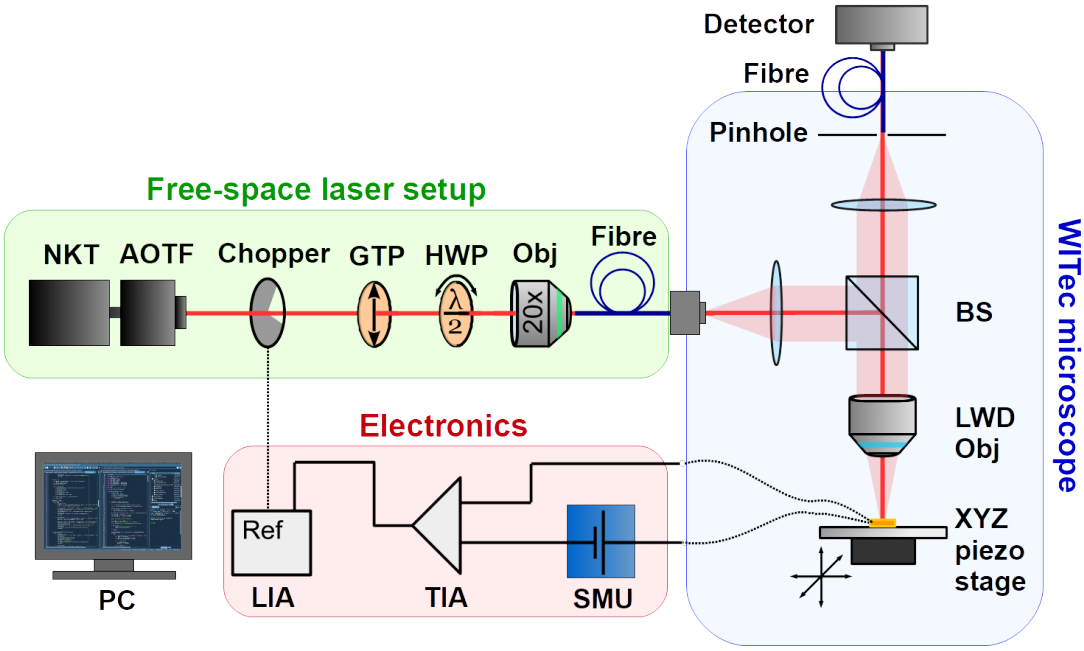

Figure 4.1: Schematic of the home-built laser setup. The following short-hand notations are used. Free-space laser setup (green): NKT = white light supercontinuum laser, AOTF = acousto-optically tuneable filter, GTP = Glan-Taylor polariser, HWP = half-wave plate, Obj = objective. Electronics (red): LIA = lock-in amplifier, TIA = trans-impedance amplifier, SMU = source measure unit. WITec microscope (blue): BS = beam splitter, LWD Obj = long working distance objective. PC = Personal computer.

4.1.1 Electronics

From right to left, the first instrument is the Keithley 2612B SourceMeter or source measure unit (SMU). The SMU provides the source-drain voltage V_{sd} for the photodetector devices and measures the resulting current I_{sd}. The compliance is the maximum allowed I_{sd} for a given V_{sd}, which we set manually to prevent extremely high currents, e.g. in case of a short-circuit. The dual-channel design of the SMU means that it can simultaneously provide gate voltages V_{G} for a FET-type device using a second channel, but this avenue is not explored in this work.

The Stanford Research Systems (SRS) SR570 Low-Noise Current Preamplifier, also known as a trans-impedance amplifier (TIA), is connected in series with the photodetector and SMU. The device is used to convert a small I_{sd} signal into a large output voltage V_{s} (maximum $\pm$5V), with sensitivities ranging from 1 pA/V to 1 mA/V. We use the SR570's default settings, except for the sensitivity, which is tuned to give a large output voltage while maintaining low noise. The SR570 TIA has two front-end amplifiers, one for low noise and one for low input currents. The low noise amplifier improves the alternating current (AC) response for sensitivities ranging from 100 nA/V to 1 mA/V. Thus, it is desirable to stay within this sensitivity range. The merits of the SR570 are its low noise (e.g. 10^{-13} A/Hz at 100 na/V sensitivity) and its low output impedance of 50 Ω.

The SR570's output is connected to the input of a SRS SR830 DSP Lock-In Amplifier (LIA), which we use to disentangle the photocurrent I_{pc} signal from I_{dark} in the total I_{sd}. For this, the LIA uses a technique called phase-sensitive detection or dual-phase demodulation, in which knowledge of the input signal's time response is used to extract its amplitude and phase from a noisy background [49]. Hence, we modulate the excitation laser at a frequency of $f_{\mathrm{r}} \approx 400$ Hz with a SRS SR540 Optical Chopper, which is connected to the reference input of the SR830. The device under test (DUT) is now illuminated periodically, producing an AC signal $V_{\mathrm{s}}(t)$ at frequency f_{s}, which we can express mathematically as:

$$\begin{aligned} V_{\mathrm{s}}(t) &= \sqrt{2} V_{\mathrm{rms}} \cos(\omega_{\mathrm{s}} t + \Theta) \\ &= \frac{V_{\mathrm{rms}}}{\sqrt{2}} \left(e^{i(\omega_{\mathrm{s}} t + \Theta)} + e^{-i(\omega_{\mathrm{s}} t + \Theta)} \right) , \end{aligned} \tag{4.1}$$

where V_{rms} is the root-mean-square (rms) amplitude, Θ is the phase of the input relative to the reference, $\omega_{\mathrm{s}} = 2\pi f_{\mathrm{s}}$ is the input signal's angular frequency, t is the time, and $i = \sqrt{-1}$. The LIA mixes V_{s} with both the in-phase reference signal and a $\pi/2$ phase-shifted (quadrature)

signal:

$$\begin{aligned} V_{\mathrm{r}}(t) &= \sqrt{2}(\cos(\omega_{\mathrm{r}}t) - i\sin(\omega_{\mathrm{r}}t)) \\ &= \sqrt{2}e^{-i\omega_{\mathrm{r}}t}\,, \end{aligned} \tag{4.2}$$

where $\omega_{\mathrm{r}} = 2\pi f_{\mathrm{r}}$. The signal after mixing is given by:

$$\begin{aligned} Z(t) &= V_{\mathrm{s}}(t) \cdot V_{\mathrm{r}}(t) \\ &= V_{\mathrm{rms}}[e^{i(\omega_{\mathrm{s}}-\omega_{\mathrm{r}})t+i\Theta} + e^{-i(\omega_{\mathrm{s}}+\omega_{\mathrm{r}})t-i\Theta}]\,. \end{aligned} \tag{4.3}$$

For $\omega_{\mathrm{s}} = \omega_{\mathrm{r}}$, the first term reduces to $e^{i\Theta}$, while the second term, the 2ω component, is removed by low-pass filtering, which is mathematically expressed as $\langle \exp[-i(2\omega t + \Theta)] \rangle = 0$. Hence, the main output of the LIA is

$$Z(t) = e^{i\Theta}\,, \tag{4.4}$$

with the absolute value $|Z| = V_{\mathrm{rms}}$ the rms signal amplitude and $\arg(Z) = \Theta$ the phase difference between the signal and the reference. On the other hand, if $\omega_{\mathrm{s}} \neq \omega_{\mathrm{r}}$, the mixed signal is no longer a simple sinusoidal function and the filtered signal averages out to zero. Thus, the consequence of dual-phase demodulation is that the LIA extracts signals coherent with the reference signal and discards all others by filtering.

The SR830 DSP uses digital mixing and filtering, allowing up to four poles of low-pass filtering, each pole contributing 6 dB/oct of filtering. In contrast, analogue RC circuits are usually limited to two poles of filtering [50]. The low pass filter's bandwidth is determined by the time constant $\tau = 1/(2\pi\Delta f)$ with $\Delta f = |f_{\mathrm{r}} - f_{\mathrm{s}}|$ the -3 dB cut-off frequency. Under normal conditions, at $f_{\mathrm{r}} = 400$ Hz, τ can be set from 10 μs to 30s in increments of 1 or 3 times 1, 10 or 100 with the appropriate units. There is a trade-off between spectral and temporal resolution, because τ determines the time it takes for the filter to settle on the final value. A single-pole filter requires about 5τ settling time, reaching up to 10τ for four-pole filtering.

The dynamic reserve determines the largest tolerable gain, i.e. the maximum noise signal to the full-scale signal, given by $20\log(V_{\mathrm{noise}}/R)$ in dB, where V_{noise} is the noise amplitude. The full scale sensitivity can be set from 2 nV to 1 V rms in increments of 1-2-5 times 1, 10 or 100 with the appropriate units. The reserve can be set to either low noise, normal, or high reserve mode, while the actual numerical reserve value in dB is set by the sensitivity. Generally, the low noise mode is desirable, but not always attainable if both the full-scale signal and noise amplitudes are large.

The amplifier noise sources can be subdivided into intrinsic and extrinsic sources. Extrinsic noise sources include capacitive coupling, inductive coupling, ground loops, microphonics and thermocouple effects. These noise sources can typically be minimised by good experiment design [50]. On the other hand, intrinsic noise sources are present in all electronic signals, e.g. Johnson noise generated due to thermal fluctuations, shot noise due to non-uniformity in the electron flow, 1/f noise, and a component at 50 Hz due to AC mains electricity. For a LIA, the most important noise source to consider is Johnson noise, which is frequency-independent and can be calculated as:

$$V_{\text{noise}} = 1.3 \cdot 10^{-10} \sqrt{R} \sqrt{ENBW}\,, \tag{4.5}$$

where R is the input impedance and ENBW the equivalent noise bandwidth. In our setup, the input impedance is determined by the SR570's output impedance, thus $R = 50\ \Omega$. The ENBW is dependent on the filter slope and τ, ranging from $1/(4\tau)$ at 6 dB/oct to $5/(64\tau)$ at 24 dB/oct. The highest signal to noise ratio is obtained when Johnson noise becomes the dominant noise source over 1/f noise, i.e. at higher modulation frequencies. We chop the laser at $f_{\text{r}} \approx 400$ Hz, because this frequency gives us the highest signal-to-noise ratio.

4.1.2 Optics

The free-space component of the home-built setup is shown in Fig. 4.2. From left to right, the first component is the NKT Photonics SuperK Extreme (NKT), which is a 78 MHz pulsed white light supercontinuum laser with wavelength range 460-2200 nm. The NKT is connected to the NKT Photonics SuperK Select acousto-optically tuneable filter (AOTF), which uses an RF driver to tune the wavelength of the NKT. The AOTF outputs a linearly polarised (horizontal with respect to the optical table) monochromatic collimated beam at the specified wavelength, with FWHM bandwidth of 3.5-14 nm in the visible (450-670 nm) or near-infrared (690-1100 nm).

The AOTF's output beam can be periodically modulated by the SRS SR540 Optical Chopper, which is connected to the LIA's reference input. Thereafter, the beam passes a Thorlabs (TL) DGL10 Double Glan-Taylor Polariser (GTP), which is mounted in a TL RSP1X15/M manual rotation mount. In this configuration, we use the GTP to produce extremely pure linear polarisation, horizontal with respect to the optical table, with an extinction ratio of 10^5:1, i.e. 90% of the horizontal polarisation is transmitted, compared to only 0.0009% for vertical

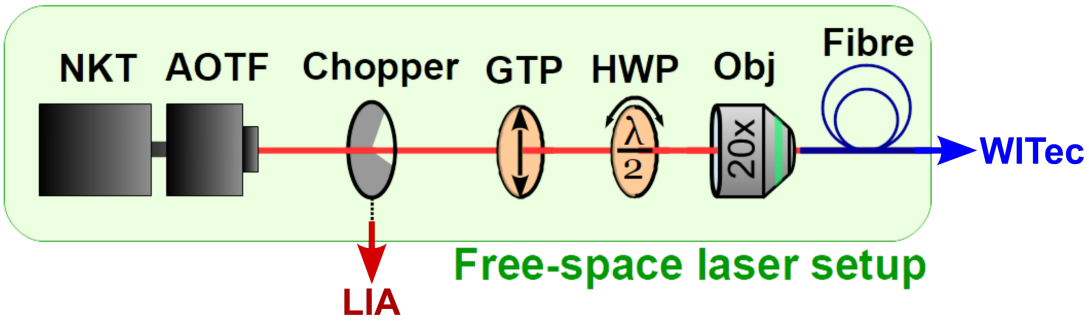

Figure 4.2: Schematic of the free-space optical setup, part of the home-built setup shown in Fig. 4.1. The following short-hand notations are used. NKT = white light supercontinuum laser, AOTF = acousto-optically tuneable filter, GTP = Glan-Taylor polariser, HWP = half-wave plate, Obj = objective. LIA = lock-in amplifier.

polarisation. Subsequently, the horizontal polarisation can be rotated by a TL AHWP05M-600 achromatic half-wave plate (HWP) mounted in a TL PRM1Z8 motorised rotation mount and controlled by a TL KDC101 Kinesis K-Cube Brushed DC Servo Motor Controller. An Olympus UplanFL N 20x objective couples the polarised beam into an NKT polarisation-maintaining photonic crystal fibre, leading to the WITec microscope. The fibre coupling is manually optimised with an XYZ translation stage.

In the WITec, the modulated laser beam is focused onto the DUT with a LWD objective. The extended working distance is necessary to avoid contact between the objective and the protruding wire bonds. We probe the DUT's absorption by measuring the photocurrent with the electronics, while the reflected light is collected by the LWD objective and out-coupled into a fibre leading to a photodetector.

For detection, we can choose either the WITec's avalanche photodiode (APD), a TL PM100USB power meter with S120C Si detector, or a TL DET100A2 large-area biased Si photodiode. The APD allows for the fastest detection, but it saturates at very low laser power and therefore requires the use of additional filters. We find no noticable difference in detection speeds of the biased photodiode and the power meter, hence we prefer to use the power meter for its straightforward measurement and readout capabilities.

4.1.3 Automation

All the electronics are connected via RS232 links to the PC, which allows us to remotely set device parameters and retrieve measured signals of the SMU and LIA. We write a Python code that automatically selects the LIA sensitivity based on the signal it receives, instead of having to manually dial it in every time. This is especially useful when a large input signal is close to overloading the amplifier, or when a tiny signal benefits from stronger amplification.

Among the optics, the NKT, AOTF, K-Cube controller and power meter are all connected to the PC via USB connections. We use custom Python programs to remotely control the excitation power, wavelength and linear polarisation, as well as to set the detection wavelength and measure the (reflected) laser power. Moreover, the WITec's piezo stage, microscope z-control and camera are also managed from the PC, with the WITec Control software functioning as proxy to remotely control the microscope using Python.

The mentioned electronics and optics are integrated into Python programs for benchmarking (fibre coupling, power spectra, polarisation calibration, knife-edge measurement) and measuring (I-V curves, photocurrent and reflection spectra and maps). The relevant settings for each of the devices are mentioned with the respective benchmarks or measurements.

4.2 Benchmarking

In this section, we start by establishing the current-voltage characteristics of two sample holders. Then, we characterise the laser power spectrum and stability, followed by the laser polarisation calibration. Lastly, we determine the radial resolution and depth of focus using a knife-edge measurement in the reflection geometry.

4.2.1 Sample holder

As discussed in section 3.5, we attach the sample to a sample holder, which is secured to a custom mount for the WITec's sample stage. An ideal sample holder should have infinite resistance, but in practice a good sample holder has a very large, but finite resistance.

We have two similar sample holders, and a picture of one of these is shown in the inset of Fig. 4.3. We measure $I-V$ curves for both holders by attaching a ribbon cable to the sample

holder, and connecting two of the pins to the source and drain terminals of the Keithley SMU. Then, we use a custom Python program to vary the SMU's bias voltage from -0.5 V to +0.5 V and back to -0.5 V in increments of 0.01 V. The current is measured 10 times at each step to minimise noise effects. Nevertheless, measurements with the SMU are very sensitive to noise when the TIA and LIA are not used to mitigate this.

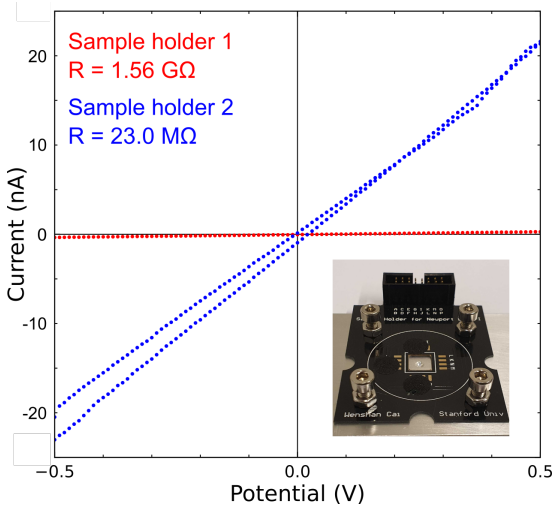

Figure 4.3: The I-V curves of the sample holders 1 (red) and 2 (blue), with the resistance obtained by fitting shown in the second quadrant, and an image of sample holder 2 secured to the custom microscope mount shown in the fourth quadrant.

The $I - V$ curves are shown in Fig. 4.3. Both sample holders show Ohmic behaviour, with noticable hysteresis, which we ascribe to capacitive coupling. Moreover, additional noise effects are likely due to microphonics, which is electrical noise caused by physical changes (e.g. vibrations) in the cables or sample holder. Clearly, there is no short circuit and sample holder 1 (red) has a much higher resistance than sample holder 2 (blue). To quantify the resistance of either holder, we fit the data to obtain the slope of each curve, which in a linear $I - V$ trace is equal to the conductance (i.e. $1/R$) by Ohm's law. The result of the fit for holder 1 is $R_1 = 1.557 \pm 0.002$ GΩ and for holder 2 we find $R_2 = 22.99 \pm 0.06$ MΩ. Since R_1 is almost two orders of magnitude higher than R_2, we exclusively use sample holder 1 from now on, to minimise the influence of leakage current in the holder.

4.2.2 Laser power

As described in section 2.1, in order to calculate a photodetector's external quantum efficiency ($EQE = I_{\mathrm{pc}}/e\Phi_\nu$) from the photocurrent, we need to know the laser wavelength and photon flux arriving at the sample. Hence, we measure power spectra before or after each set of photocurrent measurements to guarantee that the measurement conditions are the same, since the laser power is highly dependent on variations in fibre coupling and alignment of the optical elements.

We obtain power spectra by controlling the NKT, AOTF, K-Cube controller and power meter using a custom Python program that allows us to set the RF power of the AOTF, the polarisation, the wavelength range and step size, and the amount of independent power measurements at each wavelength step.

Representative spectra are shown in Fig. 4.4(a) for four different RF power percentages: 25% (red), 50% (green), 75% (blue) and 100% (magenta). The laser power of the NKT is set to 100%, the HWP angle is 0^{o}, the wavelength ranges from 460 to 670 nm with 2 nm increments, and each data point is the average of 500 measurements. Evidently, the spectral power distribution is not constant in this wavelength range due to the non-linear nature of the supercontinuum generation process. In addition, there is no simple relation between the RF power and the laser power, since the RF power influences the spatial beam profile at the output.

According to the manual [51], the AOTF output power should not deviate more than 0.5% over a period of multiple hours. Generally, acquiring spectra only takes a few seconds up to a few minutes, but photocurrent maps can take much longer, especially if the map area is very large and/or the resolution is high. Hence, we characterise the time-evolution of the laser power at the sample position to determine the stability of the entire experimental setup.

We place the power meter on the sample stage and focus the laser beam with $\lambda = 532$ nm at 50% AOTF power onto it with a 50x LWD objective. We use a custom Python program to measure the power every second over a duration of 30 minutes. The data is visualised in Fig. 4.4(b), where we normalise the data by dividing each data point by the average power, $P_{\mathrm{avg}} = 168.75\ \mu$W. The largest observed deviation from the mean is 0.61%, which is slightly larger than the value specified in the AOTF manual, but tolerable in our experiments.

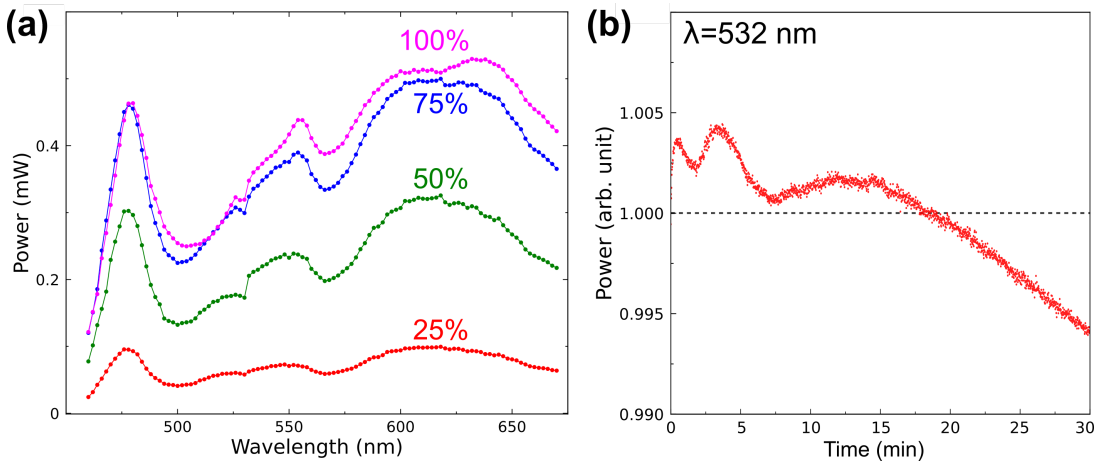

Figure 4.4: **(a)** Power spectra at the sample obtained at 25% (red), 50% (green), 75% (blue) and 100% (magenta) AOTF power. **(b)** Evolution of the laser power over time at $\lambda_{exc} = 532$ nm. The data is normalised by dividing each data point by the average power measured in the time interval. The mean is represented by the dashed line.

4.2.3 Polarisation calibration

The AOTF's output is linearly polarised and horizontally oriented with respect to the optical table. In the normal configuration, shown in Fig. 4.2, the GTP's polarisation axis is aligned with the AOTF output. The HWP is mounted in a motorised rotation mount to rotate the polarisation by any angular amount with an accuracy of 0.01°. Figure 4.5(a) shows the operating principle of a HWP. Consider an incoming wave (blue) that is linearly polarised at an angle θ with respect to the HWP's major axis (green). The output polarisation (red) will be rotated by 2θ, due to the birefringence of the HWP crystal.

The first step of polarisation calibration consists of aligning the HWP's optical axis with the polarisation transmitted by the GTP. We achieve this by reversing the order of the HWP and GTP in the free-space laser setup (Fig. 4.2) and placing the power meter in the beam path after the GTP. We use a custom Python program to rotate the HWP from 0° to 360° in 2° increments, and measure the power at each HWP angle. The measured power is largest when the HWP's output polarisation is aligned with the GTP, while reaching a minimum when it is orthogonal with the GTP. The power as function of HWP angle is shown in Fig. 4.5(b).

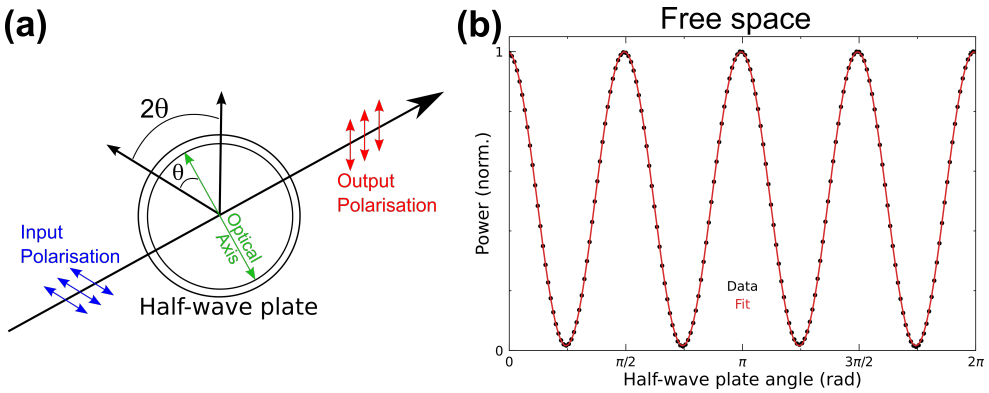

Figure 4.5: **(a)** Schematic of a HWP. The input polarisation (blue) is rotated by 2θ to produce output polarisation (red), with θ the angle between the input polarisation and the optical axis. **(b)** Normalised power as function of HWP angle, measured after the GTP in free-space.

We fit the data (black dots) with a cosine function (red line) to find a phase shift of -1.18°, which means that the HWP is offset by -1.18° with respect to the GTP polarisation axis. In other words, the HWP angle must be $\theta_{\text{hor}}(n) = -1.18^{\text{o}} \pm n \cdot 90^{\text{o}}$ with integer n to produce horizontal polarisation with respect to the optical table, and $\theta_{\text{ver}}(n) = -1.18^{\text{o}} \pm (2n+1) \cdot 45^{\text{o}}$ to produce vertical polarisation. From now on, this offset correction is implicit when discussing the HWP angle.

Although this is valuable information, we are mostly interested in the polarisation at the sample position, which may be different due to, for instance, the fibre-coupling or the microscope objective. We determine the polarisation at the sample position with a procedure similar to the free-space polarisation calibration. First, the GTP is moved to its original position before the HWP and the power meter is placed on the sample stage. We measure the power as function of HWP angle from 0° to 180° with steps of 2°. The power is dependent on the HWP angle, because slight imperfections in the mounting of the HWP lead to changes in fibre coupling upon rotation.

We use a TL WP25M-VIS Wire Grid Polariser to determine the polarisation orientation at the sample. The wire grid transmits light with in an electric field vector perpendicular to the wires (parallel to the polarisation axis), while reflecting orthogonally polarised light, with an extinction ratio of 800:1.

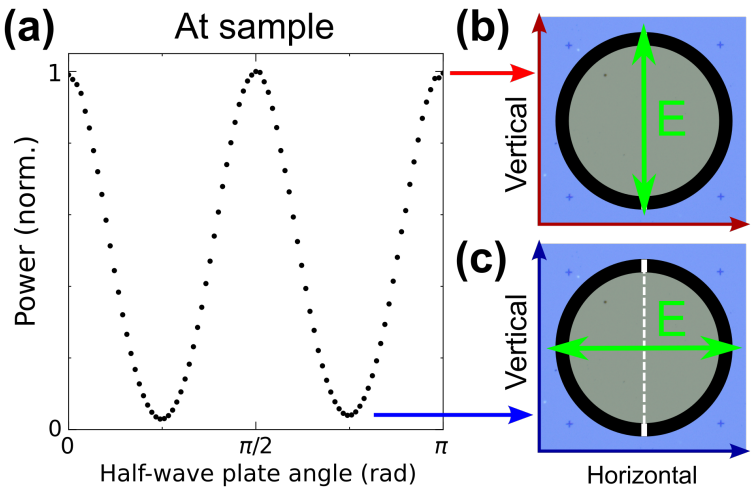

Figure 4.6: **(a)** Normalised power as function of HWP angle, polarised with a wire grid polariser at the sample position. **(b, c)** Illustrations of the wire grid polariser overlaid on the WITec's video image, with the electric field vector (E, green) parallel and perpendicular to the wire grid's polarisation axis (white, dashed), respectively. The horizontal and vertical axes of the video image are indicated.

We place the wire grid on top of the power meter and manually align its polarisation axis with the vertical axis of the microscope's video image. This is illustrated in Fig. 4.6(b) and (c), with the white dashed line in (c) indicating the wire grid's polarisation axis. Now, with the polariser in place, we measure the power spectrum again. We divide the result by the unpolarised power data, normalise it, and plot it in Fig. 4.6(a). As indicated by the arrows, the transmission reaches a maximum (minimum) when the polarisation of the laser is aligned parallel (perpendicular) with the wire grid's polarisation axis, and thus with the vertical (horizontal) axis of the microscope's video image. Since the maxima are obtained for HWP angles of 0, $\pi/2$ and π, we conclude that a horizontally polarised beam in free-space (with respect to the optical table) corresponds to a vertically polarised beam at the sample position (with respect to the microscope's video image) and vice versa.

4.2.4 Resolution and depth of focus

We characterise the radial resolution and depth of focus of the setup using the knife-edge technique. Central to this technique is the paraxial approximation of a Gaussian beam.

Consider a laser beam with a Gaussian transverse irradiance profile propagating in the z direction, as shown in Fig. 4.7(a) and expressed as [52]:

$$I(r,z) = I_0(z)\, e^{-4\rho^2/w^2(z)} \propto |\mathcal{E}_{00}(\rho,z)|^2\,, \tag{4.6}$$

with beam radius $w(z)$, radial distance $\rho = \sqrt{x^2+y^2}$, and electric field amplitude $\mathcal{E}_{00}(\rho,z)$. The minimum spot size is known as the beam waist w_0 and is located at $z = 0$ by definition. In the far-field, the Gaussian beam diverges with the divergence angle:

$$\Delta\theta = \frac{\lambda}{\pi n w_0}\,. \tag{4.7}$$

On the other hand, the beam remains well collimated within the Rayleigh range:

$$z_R = \frac{\pi n w_0^2}{\lambda}\,. \tag{4.8}$$

Using this definition, we can express $w(z)$ as:

$$w(z) = w_0\sqrt{1+\frac{z^2}{z_R^2}}\,. \tag{4.9}$$

The spot size $w(z)$ is related to the full width at half maximum as $\mathrm{FWHM}(z) = \sqrt{2\ln 2}\cdot w(z)$.

The goal of the knife-edge method is to obtain w_0 and use this to calculate the remaining beam parameters. We focus the 50x LWD objective on a sapphire (Al_2O_3) substrate with an aluminium (Al) microscale electrode functioning as the knife-edge, as shown in Fig 4.7(b). We illuminate the knife-edge with the NKT laser at $\lambda = 500$ nm and scan the laser spot horizontally (x-direction) over the knife-edge, represented in Fig. 4.7(b) by the red line. The Al is highly reflective, but the sapphire barely reflects any light. Thus, the reflected power is maximal, $P_{\max}$, when the laser beam is positioned on the Al and decreases as the laser moves away from the knife-edge, reaching a minimum, $P_{\min}$, when the laser solely illuminates the sapphire substrate.

We use a custom Python program to scan in the x-direction with 50 nm steps, measure the reflected power at each step, and repeat this process for -2 μm $\leq z \leq$ 2 μm with 50 nm increments. Here, a negative z means that the focus is above the surface, and positive z corresponds to the focus below the surface.

At every z, we fit the detected power with:

$$P(x,z) = P_{\min} + \frac{P_{\max}}{2}\left(1-\mathrm{erf}\left(\frac{2(x-x_0)}{w(z)}\right)\right)\,, \tag{4.10}$$

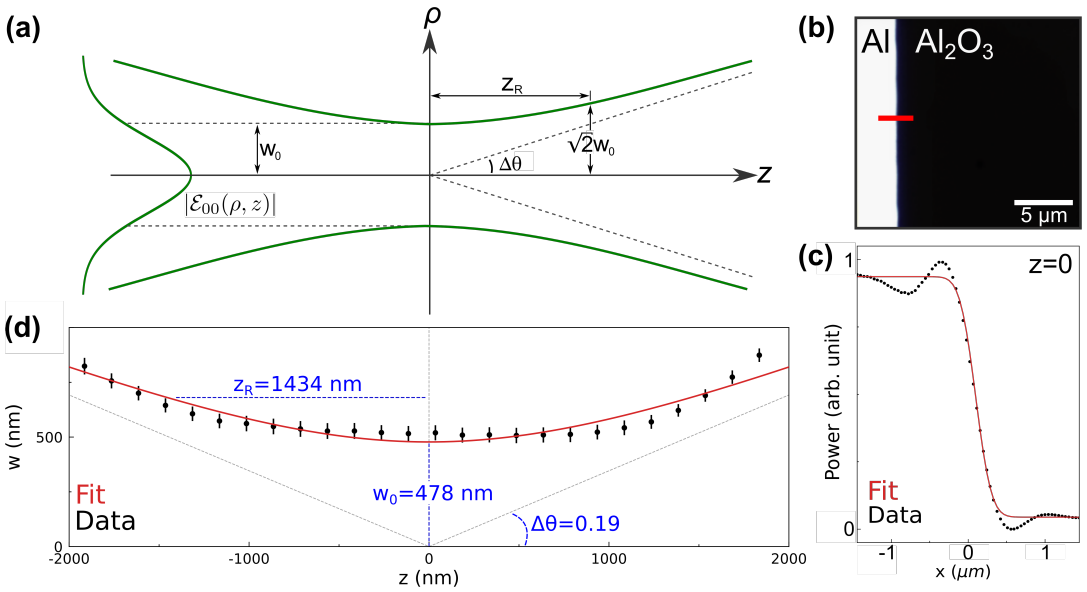

Figure 4.7: **(a)** Schematic of the Gaussian beam (green), inspired by [52]. **(b)** Optical microscope image of the Al electrode on a sapphire substrate. The red line indicates the lateral scanning direction. **(c)** Reflected power (normalised) when scanning the laser laterally over the knife edge at $z = 0$. The black dots are the data points and the red line is the fit. **(d)** Plot of $w(z)$ data (black dots) obtained by fitting $P(x)$ for all z values, with the error bars (black lines) indicating the standard deviation of the fits. The data is fitted (red curve) with Eq. 4.9 to obtain w_0 and calculate z_R and $\Delta\theta$ (all indicated in blue).

where x_0 is the x-coordinate where the power equals $(P_{\min} + P_{\max})/2$, and erf is the error function, resulting from the convolution of a Gaussian line shape with a step function [53]:

$$\mathrm{erf}(a) = \frac{2}{\sqrt{\pi}} \int_0^a e^{-u^2} \mathrm{d}u \,. \tag{4.11}$$

The data (black dots) and fit (red line) for $P(x, z = 0)$ is shown in Fig. 4.7(c). The discrepancy between the data and the fit is because in reality a diffraction-limited laser beam is not a Gaussian, but an Airy disk, which has additional higher-order diffraction maxima. Hence, the oscillations at $P_{\min}$ and $P_{\max}$ are caused by the side lobes of the Airy pattern.

We extract $w(z)$ (black dots) and the standard deviation (error bars) from each of the $P(x, z)$ fits, and plot this in Fig. 4.7(d). We fit (red line) the data with Eq. 4.9. The discrepancy

between the data and the fit is the greatest at large positive z, because here the focal point inside the substrate, leading to aberrations in the reflected image. From the fit we find $w_0 = 478 \pm 7$ nm, and we use this to calculate the other beam parameters.

For the beam divergence, we find $\Delta\theta = 0.19 \pm 3 \cdot 10^{-4}$ rad. The paraxial approximation requires that $\sin(\Delta\theta) \approx \Delta\theta$, in our case $\sin(0.19) \approx 0.189$, thus the approximation is valid. The Rayleigh range is equal to $z_R = 1434 \pm 44$ nm. Now, the depth of focus is usually defined as $2z_R$, which means that a beam with $\lambda_{\text{exc}} = 500$ nm remains well collimated within ± 1.43 μm from the optimal focus. We find FWHM$(0) = 562 \pm 9$ nm and compare this to the Abbe diffraction limit [53]:

$$\rho_{||} \geq 0.6098 \frac{\lambda}{\text{NA}}\,, \tag{4.12}$$

where $\text{NA} = n \sin(\theta)$ is the numerical aperture of the focusing objective. The 50x LWD objective has NA $= 0.55$, thus the Abbe limit $\rho_{||} \geq 554$ nm. Evidently, the spatial resolution of the experimental setup is diffraction-limited within the FWHM error margin.

Now that the setup is fully calibrated and characterised, we proceed with measurements on a state-of-the-art resonant photodetector in the following chapter.

Chapter 5

Si nanowire array photodetector

Before we commence with the investigation of the WS_2 photodetectors, we first benchmark the home-built setup for the characterisation of resonant nanoscale photodetectors. To this end, we use transparent Si nanowire (NW) arrays. These arrays are designed and fabricated at Stanford University by Li and co-workers [3], who have successfully demonstrated the use of these Mie resonant metasurfaces as transparent spectropolarimetric photodetectors. The authors have also carried out simulations on the optical performance of the NWs to verify their experimental results. Hence, these photodetectors provide an ideal testing ground for our home-built setup, allowing us to benchmark it for spectrally and polarisation-resolved optical and optoelectronic measurements.

In the following, we first explain the principles of transparent Si NW photodetectors (5.1). Next, we prepare the sample by mounting and wire bonding it to our custom sample holder, and we confirm the electrical contacts by measuring an $I-V$ characteristic (5.2). Thereafter, we measure polarisation-resolved spectra and maps of the EQE (5.3) and the reflectance (5.4). Finally, we discuss the potential for colour detection by measuring the reflectance spectra for multiple NW arrays (5.5). It should be explicitly noted that all the experimental data presented in this chapter is measured by us, while all the simulations are performed by Li and co-workers.

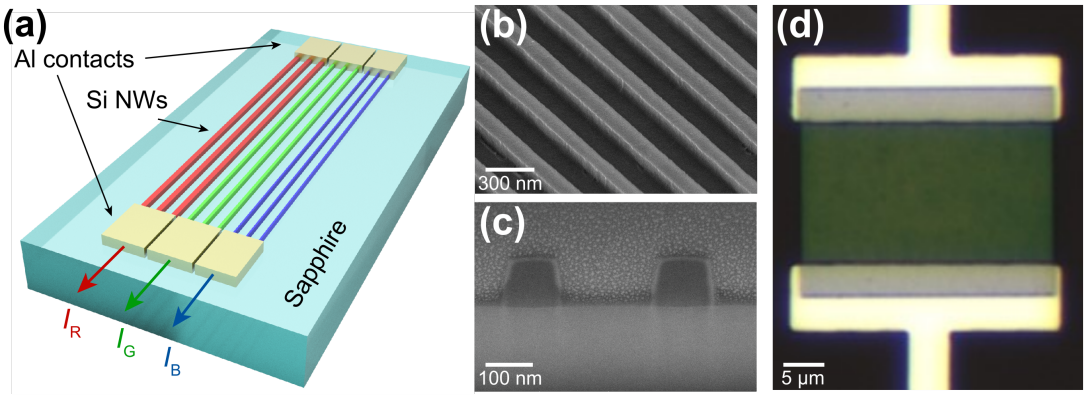

Figure 5.1: **(a)** Transparent multispectral photodetector concept consisting of three different Si NW arrays on a sapphire substrate with aluminium (Al) contacts for extraction of the photogenerated charge carriers. **(b)** Tilted-view and **(c)** cross-sectional SEM images of the "red" NW array. **(d)** Optical microscope image of the "red" NW array photodetector.

5.1 Background

Figure 5.1(a) shows a schematic of transparent Si NW arrays designed for the detection of red, green and blue light. The arrays are fabricated on a sapphire substrate and have aluminium source and drain contacts. All of the NWs have a height of $h = 110$ nm, while the width and spacing period of the wires is used to tune the resonant detection wavelength. Panels (b) and (c) show tilted-view and cross-section scanning electron microscope images, respectively, of the "red" NW array with a width of $w = 110$ nm and a period of $p = 310$ nm. Counter-intuitively, the "red" array looks green when observing it with an optical microscope, as shown in Fig. 5.1(d). This is because the device is designed for simultaneous resonant absorption and antireflection of red light. As a result, the absorption (reflection) is weakest (strongest) for green light. This can be seen in Fig. 5.2(a), which shows the simulated absorbance spectra of "red" (R), "green" (G) and "blue" (B) NW photodetectors. The combination of these three NWs into a single detection pixel, like the schematic shown in Fig. 5.1(a), mimicks the human visual system, with distinct but overlapping absorption maxima allowing for efficient colour detection.

The NWs are optimised for detection of light with transverse magnetic (TM) polarisation, which is defined as the electric field component of the incident light oriented parallel to the NW

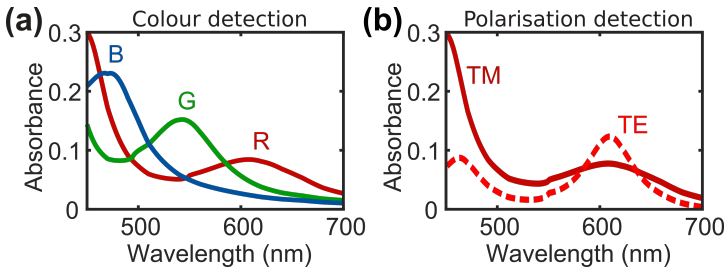

Figure 5.2: **(a)** Simulated absorbance spectra for TM-illumination of NW arrays designed for the detection of red (R), green (G) and blue (B) light. **(b)** Simulated absorbance spectra for the "red" photodetector under illumination with TE and TM-polarised light.

axis. On the other hand, the devices should show anti-reflection behaviour for the orthogonal transverse electric (TE) polarisation. However, it turns out that the TM and TE resonances are nearly degenerate for the "red" NWs, as shown in the simulated absorbance spectra of Fig. 5.2(b). Consequently, polarisation detection is relatively inefficient with this device, as discussed comprehensively in section 5.3.

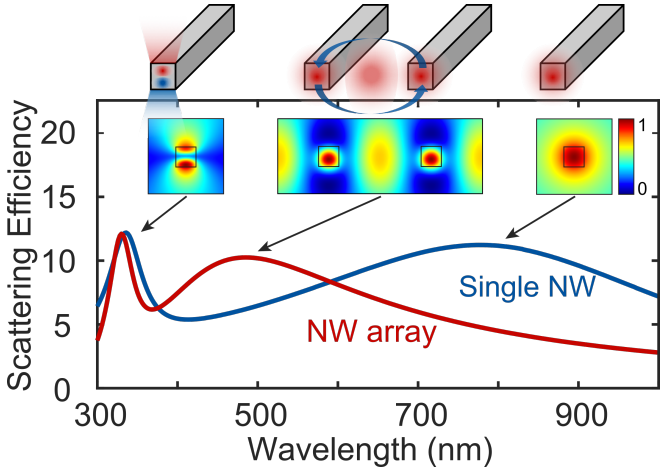

Figure 5.3: Scattering efficiency spectrum for a NW (blue, $w = h = 55$ nm) and an array of such NWs (red, $p = 280$ nm) under TM-polarised illumination, calculated as the ratio of the scattering and geometrical cross-sections. The insets show the modulus of the scattering electric field distribution $|E_{\mathrm{sca},z}|$ at the second-order resonance for a single NW (left) and the first-order resonance of the NW array (middle) and single NW (right).

The working principle of the NW photodetectors is based on Mie resonances and tailoring of the radiative coupling between adjacent NWs. To understand this, consider the simulated scattering efficiency spectra (for TM-polarised light) of a single NW (blue) with $w = h = 55$ nm, and an array of such NWs with a spacing of $p = 280$ nm, illustrated in Fig. 5.3. The single NW features a first-order resonance in the infrared with an omnidirectional field profile (inset), and second-order mode in the ultraviolet with an asymmetric out-of-plane radiation pattern (inset). In the array, the in-plane radiation gives rise to a first-order resonance which is significantly blueshifted compared to the resonance of the single NW. The field distribution near the resonance peak (inset) indicates that this is a different type of resonance where light is scattered between adjacent NWs. As a result of this radiative coupling, the resonance wavelength can be tuned by varying the spacing between the NWs. The coupling between NWs is negligible for the second-order mode due to the out-of-plane field profile. Hence, the spectral position of the first-order resonant mode can be shifted independently from the second-order mode, facilitating the creation of NW arrays with optical resonances at any wavelength in the visible range. The overall back-scattering amplitude and phase are engineered to destructively interfere with the direct reflection component. This gives rise to effective anti-reflection at resonance.

5.2 Current-voltage characteristic

The aluminium source and drain contacts of the "red" NW array are contacted in a lithographic process similar to the one described in section 3.5. The contacts terminate in 150×150 μm^2 contact pads, as is visible in Fig. 5.4(a). The sapphire substrate with NW arrays is situated on a gold chip, with wire bonds interconnecting the contact pads of the "red" device and the gold chip. In the following, we simply use "device" to refer to the NW array designed for red light.

We attach the gold chip with double-sided tape to the sample holder, as shown in the inset of Fig. 5.4(b). Next, we wire bond the chip to the holder to facilitate electrical measurements. Finally, we secure the sample holder to the custom mount for the WITec microscope.

We measure the $I - V$ characteristic, plotted in Fig 5.4(b), in a procedure identical to the one described in 4.2, except for a larger range of bias voltages, from -1V to +1V. The measured data (blue) shows mostly linear behaviour, indicating good Ohmic contact and confirming that

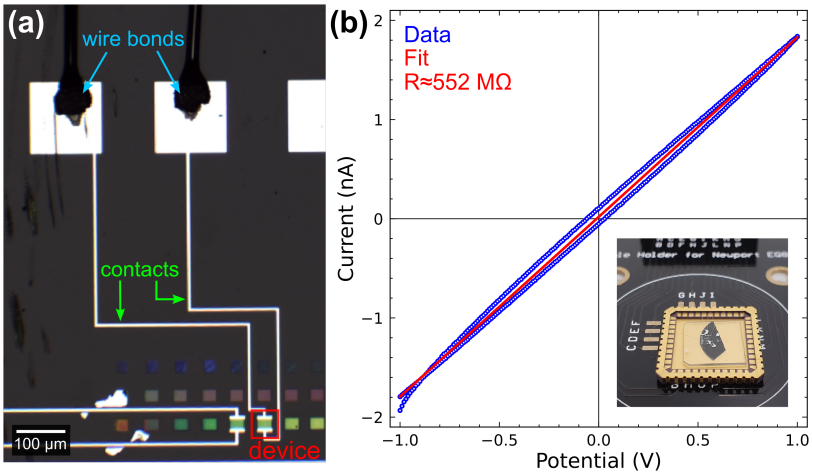

Figure 5.4: **(a)** Optical microscope image of the "red" NW array device (indicated in red) with aluminium contacts (green) and wire bonds (blue). **(b)** Measured $I - V$ characteristic of the device (blue). The linear fit (red) yields $R \approx 552$ MΩ. The inset shows the gold chip with the NW arrays attached to the sample holder.

the electrical circuit is closed, but not shorted. Similar to the bare sample holders (section 4.2), we attribute the hysteresis to capacitive coupling.

From fitting the data (red) we obtain $R = 552.1 \pm 1.6$ MΩ. Although this is a large resistance, this poses no problem because the sample holder's resistance, ~ 1.56 GΩ (section 4.2.1), is almost three times as large. In comparison, the other sample holder has a resistance of only ~ 23 MΩ. If we had used this one instead, the current would flow through the holder rather than the device, thereby preventing any electrical measurements on the device.

5.3 Polarisation detection

This section discusses the detection of TM and TE-polarised light with the device. First, we determine the external quantum efficiency to probe the polarisation-dependent resonant absorption of the device. Thereafter, the EQE data is corroborated by reflection maps and spectra, which we also compare to simulations and to spectra acquired using a white light halogen lamp.

5.3.1 External Quantum Efficiency

We use the external quantum efficiency to assess the polarisation-dependent absorption of the device. The EQE spectra are calculated by combining photocurrent and laser wavelength and photon flux according to Eq. 2.3. Assuming the IQE to be wavelength-independent in the visible range, the EQE becomes linearly dependent on the absorption efficiency (Eq. 2.4).

We acquire TM and TE-polarisation spectra from 460 to 670 nm in 2 nm increments, with 75% AOTF power and modulation by the chopper wheel at $f_r \approx 400$ Hz. We apply a bias voltage of 1.5V to extract the photogenerated charge carriers, set the TIA sensitivity to 100 nA/V, and measure the resulting AC current with the LIA. For the LIA we use our optimised auto-sensitivity routine, with the initial full-scale sensitivity set to 10 mV (=1 nA). Furthermore, we set dynamic reserve to normal mode, and use a filter slope of 24 dB/Oct with $\tau = 100$ ms and 1 s delay for the filter to settle to the final value.

The EQE spectra for TM (red) and TE (blue) polarisation are plotted in Fig. 5.5(a), with the green marker in the inset indicating the location where the spectra are acquired. Comparing the EQE spectra to the simulated absorbance spectra in Fig. 5.2(b), we clearly see the "red" device's dominant TE resonance near 600 nm. The peak position does not correspond exactly to the simulated data, which we attribute to slightly different geometrical parameters used in the simulations. The TM spectrum deviates more from the simulated absorbance spectrum. This may be due to misalignment of the excitation polarisation and the NW axis, resulting in partial excitation of the TE resonance and thereby warping the TM spectrum. This result is not as noticeable in the TE spectrum because this resonance has a higher quality factor.

Appearing as black vertical lines on the right side of the array, shown in the inset of Fig. 5.5(a), are defects that have arisen for an unknown reason. Possibly, the damage can be traced back to overheating of certain NWs as a result of excessive current densities. The defects should not impact our measurements, because the radiative coupling is only between adjacent NWs and the spectra are acquired away from the damaged region, as indicated by the green marker. We investigate the spatial variation in the photocurrent signal produced by the device to verify that the defects do not influence the measured spectra.

We acquire spatially resolved EQE maps at $\lambda = 575$ nm to yield a large contrast between the TE and TM maps. At this wavelength, with the parameters described above, the average

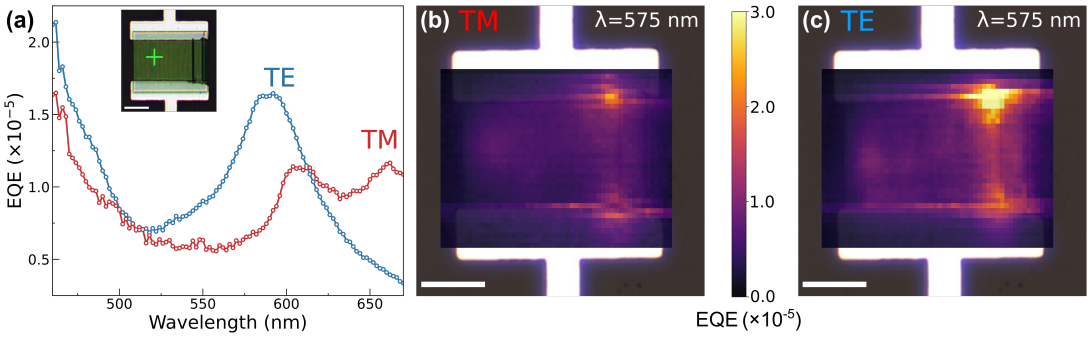

Figure 5.5: **(a)** Measured EQE spectrum for TM (red) and TE (blue) polarisation. The inset shows the NW array with the defects appearing as black lines and the green marker indicating the position the spectra were obtained. **(b)** TM and **(c)** TE polarisation EQE maps at $\lambda = 575$ nm, superimposed on optical microscope images of the "red" NW array photodetector. Scale bars: 10 μm

power arriving at the sample is 0.54 mW for TE-illumination and 0.30 mW for TM-illumination, which we use to calculate the EQE from the measured photocurrent signal. Each map consists of 1352 pixels covering an area of 38.2×29.7 μm^2, hence the resolution is ~ 0.6 μm^2/pixel.

To avoid exceedingly long acquisition times, we reduce the filter time constant to 30 ms and the wait time to 300 ms. The data is superimposed on optical microscope images of the device in Fig. 5.5(b) and (c) for TM and TE-illumination, respectively. Evidently, the defect has a considerable impact on the EQE in regions surrounding it. Especially for TE-polarised light, the EQE reaches over $5.5 \cdot 10^{-5}$ near the defect, which is more than three times larger than the EQE at resonance in the TE spectrum shown in panel (a). Nevertheless, the EQE far away from the defect is unaffected by it, and reasonably uniform for both polarisations.

It should be noted that the electrical contacts for the device are not optimised to produce large photocurrents, hence the low EQE on the order of 10^{-5}. Instead, the device is fabricated to demonstrate the concept of Mie-resonant NW arrays as spectropolarimetric photodetectors. As such, the measured spectral shapes match those from the simulations and the generated photocurrent (away from the defect) is sufficiently uniform. Importantly, we successfully demonstrate the capability to measure spatially and polarisation-resolved EQE maps and spectra with our home-built setup.

5.3.2 Reflectance

When acquiring photocurrent maps with our home-built setup, the back-scattered light is captured by the 50x objective and detected with the power meter. We measure the reflected photon flux Φ_ν to correlate map coordinates with the corresponding position on the sample and to straightforwardly spot issues with alignment of the sample and/or the laser.

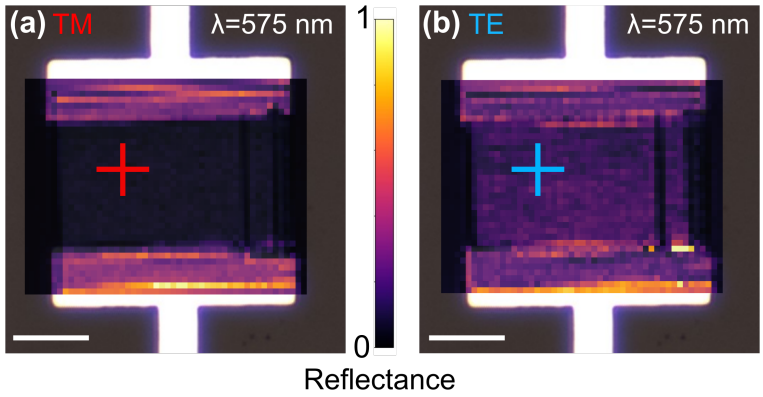

Figure 5.6: **(a)** TM and **(b)** TE-illumination reflection maps acquired at $\lambda = 575$ nm, simultaneously with the photocurrent maps of Fig. 5.5(b) and (c), respectively. The coloured markers indicate the acquisition positions of the spectra presented in Fig. 5.7(a). Scale bars: 10 μm

Figure 5.6(a) and (b) show the reflection maps acquired for TM and TE-polarised light with $\lambda = 575$ nm, measured simultaneously with the photocurrent maps of 5.5(b) and (c). The reflectance is normalised as $R = \Phi_\nu/\Phi_\nu^{\max}$, with $\Phi_\nu^{\max}$ the maximum reflected photon flux measured on the aluminium contacts. Figure5.6(a) clearly shows the that the NWs barely reflect TM-polarised light at resonance. In contrast, the TE map of Fig. 5.6(b) reveals that the NW array strongly reflects TE-polarised light.

To further investigate this, we use the home-built setup to measure polarisation-resolved reflectance spectra, shown in Fig. 5.7(a). The spectra are acquired from 460 to 670 nm in 1 nm increments, measured at the same position as the EQE spectra of Fig. 5.5(a), indicated by the red (TM) and blue (TE) markers in Fig. 5.6(a) and (b). Unlike the maps, the reflectance spectra are not obtained simultaneously with the EQE spectra, because the modulation of the chopper wheel introduces unwanted artefacts in the measured photon flux. Normalisation is achieved by measuring the photon flux reflected from a TL PF10-03-P01 protected silver

mirror, Φ_ν^{ref}, and the dark counts, Φ_ν^{dark}. The reflectance is then calculated as:

$$R = \frac{\Phi_\nu - \Phi_\nu^{\text{dark}}}{\Phi_\nu^{\text{ref}} - \Phi_\nu^{\text{dark}}} \cdot R_{\text{theory}}^{\text{ref}} \,, \tag{5.1}$$

where $R_{\text{theory}}^{\text{ref}}$ is the reference mirror's theoretical reflection spectrum obtained from Thorlabs.com. The spectra clearly show the origin of the reflection contrast between TM and TE-polarised light. The TM spectrum has a reflection minimum near 625 nm, as the NW arrays are designed to scarcely reflect TM-illumination at resonance. On the other hand, the NW array clearly has non-perfect antireflection behaviour for TE polarisation, with a large peak in the spectrum near 575 nm.

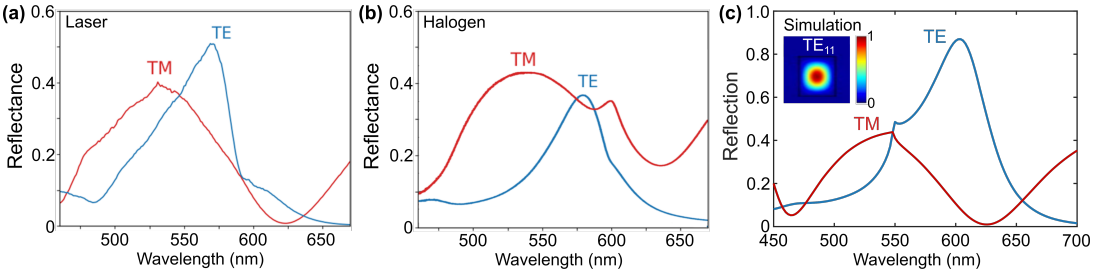

Figure 5.7: **(a)** TM (red) and TE (blue) polarisation reflectance spectra, measured with the home-built setup. The red and blue markers in (a) and (b) indicate the acquisition position of the TM and TE spectra, respectively. **(b)** TM (red) and TE (blue) polarisation reflectance spectra, measured with the white light halogen lamp and spectrometer. **(c)** Simulated reflection spectra under TM (red) and TE (blue) illumination. The inset shows the first-order TE resonance which causes the large peak in the TE spectrum.

Generally, the WITec microscope allows for more straightforward and higher-resolution reflection measurements by using a white light halogen lamp (Zeiss HAL 100) for illumination, the analyser for polarisation, and the spectrometer and CCD for detection. In order to check the data obtained with the home-built setup, we use the WITec to measure the TM and TE-polarised reflectance spectra with a spectral resolution of ~ 0.082 nm, as shown in Fig. 5.7(b). Although the spectral shapes show similarities to those in (a), they are marked by large differences. Comparing (b) to (a), we observe no minimum near 625 nm for TM polarisation, and the peak near 575 nm in the TE spectrum is much smaller. Moreover, the TM spectrum shows a wiggle near 600 nm, which is caused by a guided mode resonance and will be discussed in the next section.

Finally, we compare our data with the simulated spectra shown in 5.7(c). The spectra acquired with our home-built setup show excellent agreement with the simulations. The inset shows the first-order TE resonance, which causes the large peak in the TE spectrum. Apart from the TM guided mode resonance, we attribute the discrepancy between the halogen spectra and simulations to faulty normalisation caused by slight differences in the objective's focus on the NW array and the reference mirror.

Although here we obtain better correspondence to the simulations with our home-built setup, it suffers equally from difficulties with normalisation. Moreover, the spectral resolution is limited by the AOTF bandwidth and acquisition is relatively slow, because each measurement must be repeated several times to mitigate the effects of noise. In contrast, the spectrometer and CCD allow us to measure higher-resolution spectra with a larger spectral range and greater throughput. Hence, we preferably use this technique for reflection spectroscopy and, as we will see in the following section, the halogen lamp and spectrometer can be used to achieve an excellent match with the simulated data.

5.4 Colour detection

There are many uncontacted NW arrays on the substrate, of which a selection is shown in the inset of Fig. 5.8(a), with variations in the widths and spacings of the NWs causing the different apparent colours. We cannot show the full colour detection capability of a detection pixel, shown in Fig. 5.1(a), because for this we must measure the EQE of "blue" and "green" devices, but only the "red" array is electrically contacted. Hence, in this section we investigate colour detection by comparing the reflectance spectra of the ("red") device with those of NW arrays designed for green and blue.
Figure 5.8(a) displays the reflectance spectra obtained with the halogen lamp and spectrometer for the device and the NW arrays designed for green and blue, under TM-illumination. For comparison, we also plot the substrate reflectance spectrum (brown) and the TE spectrum for the "green" array (dark green, dashed). The NW arrays we use to measure the "green" and "blue" spectra are indicated in the inset of (a).

Figure 5.8(b) shows the simulated spectra of "red" ($w = 110$ nm, $p = 310$ nm), "green" ($w = 55$ nm, $p = 280$ nm) and "blue" ($w = 30$ nm, $p = 230$ nm) NW arrays, with the simulated first-order TM reflection minima indicated by the red, green and blue triangles in Fig. 5.8(a).

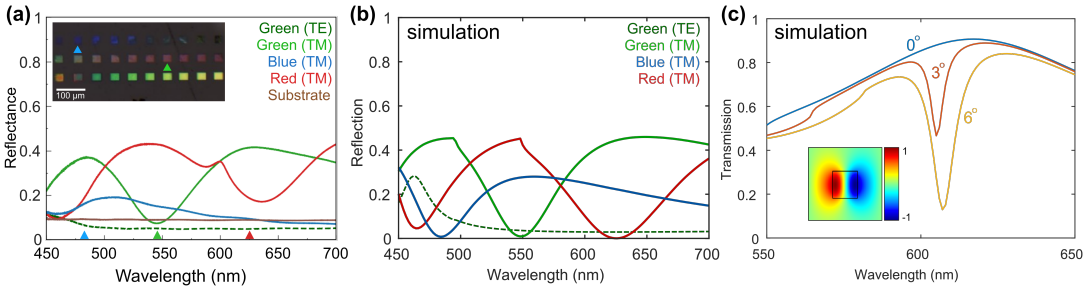

Figure 5.8: **(a)** Reflectance spectra for "red", "green" and "blue" NW arrays (with the triangles indicating the reflection minima from the simulations) and the substrate, measured with the halogen lamp and spectrometer. The inset shows several fabricated NW arrays, with the blue and green triangles indicating the arrays where the "blue" and "green" spectra are measured, respectively. **(b)** Simulated reflection spectra for "red", "green" and "blue" NW arrays. **(c)** Simulated transmission spectra for TM-illumination with 0° (blue), 3° (orange) and 6° (yellow) angle of incidence. The valley under off-normal incident illumination are caused by excitation of the guided mode resonance. The inset shows the electric field distribution of the guided mode resonance under normal incident illumination.

Overall, the measured spectral shapes show good agreement with the simulations. The best correspondence is observed for the "green" array, while the measured reflection minimum for the "blue" and "red" array are shifted towards the ultraviolet and infrared, respectively. For the "blue" NWs, we attribute this to differences in the geometrical parameters of the measured and the simulated arrays. The simulated reflectance of the "red" NW array closely matches the spectrum measured with our home-built setup, shown in Fig. 5.7(a), indicating that the observed mismatch between the simulated and halogen-illuminated spectra has another origin.

The wiggle observed in the "red" TM spectrum is traced back to a guided mode resonance that can be excited at off-normal incidence. The simulated spectra in Fig. 5.8(b) are acquired for normal incidence illumination, thus the guided mode resonance is not excited. Figure 5.8(c) shows the simulated transmission spectra for the "red" NW array for different angles of incidence, with the inset showing the field distribution of the guided mode resonance under normal incidence illumination. The anti-symmetric radiation profile means that the guided mode resonance is "dark" for normal incident TM-polarised light. In contrast, the mode becomes bright under off-normal illumination, giving rise to the sharp valleys observed in the simulated transmission spectra with 3° and 6° angle of incidence.

In the halogen-illumination reflectance spectrum of the "red" NW array, we use a 50x objective with numerical aperture NA= 0.55. This corresponds to a maximum incidence angle of $\sim$ 16.7 ^{o}, thus giving rise to the guided mode resonance by off-normal excitation. We do not observe this resonance for the "green" and "blue" NWs, because for these arrays the mode is blue-shifted to wavelengths shorter than 450 nm. Notably, we do not excite the guided mode resonance with our home-built setup, even though we use the same 50x objective. We attribute this to the non-local character of the guided mode resonance. The laser in the home-built setup is focused to a diffraction-limited spot, exciting only a few NWs at the same time. In contrast, many NWs are illuminated simultaneously with the white-light halogen lamp, resulting in the excitation of the guided mode resonance.

Altogether, we have demonstrated that the home-built setup can be used to great effect for polarisation-resolved photocurrent spectroscopy. Moreover, we have shown the ability to simultaneously measure spatially resolved EQE and R maps, which is very useful to correlate the measured data to the position on the sample. Lastly, we have utilised the WITec with a halogen lamp to further elucidate the spectropolarimetric photodetection capacity of the Mie-resonant NW arrays.

Chapter 6

2D WS_2 photodetectors

In this chapter, we investigate the 2D WS_2 photodetectors fabricated and discussed in chapter 3. First of all, we examine the electrical circuit by measuring the $I-V$ characteristics (6.1). Next, we acquire the external quantum efficiency (6.2) and reflectance (6.3) spectra to determine the role of excitons on the optoelectronic and optical properties of the devices, respectively. Finally, we measure EQE and reflectance maps to study spatial variation in the signal at the A exciton resonance wavelength (6.4).

6.1 Current-voltage characteristics

The source and drain contacts of the two devices are electrically connected to the sample holder's contact pads. Each of the pads is labelled with a letter, and we refer to the devices correspondingly as "GH" and "IJ". We obtain $I-V$ curves with the SMU by varying the voltage incrementally from -0.5V to +0.5V and back, with a step size of 0.01 V. At each step we measure the current ten times to mitigate the influence of noise on the measurements. We plot the $I-V$ curves in Fig. 6.1(a) and (b), where the data is represented in blue and the fits are indicated in green and red for devices "GH" and "IJ", respectively.

Focusing first on "GH", we obtain $R = 1.49 \pm 0.01$ MΩ from the fit. In this case, the linear fit may be inappropriate due to the asymmetry observed near +0.25 V, which we attribute to a small Schottky barrier at the semiconductor-metal interface [11, 26]. Next, for device "IJ" we observe slight capacitive coupling-induced hysteresis, but we do not observe asymmetric

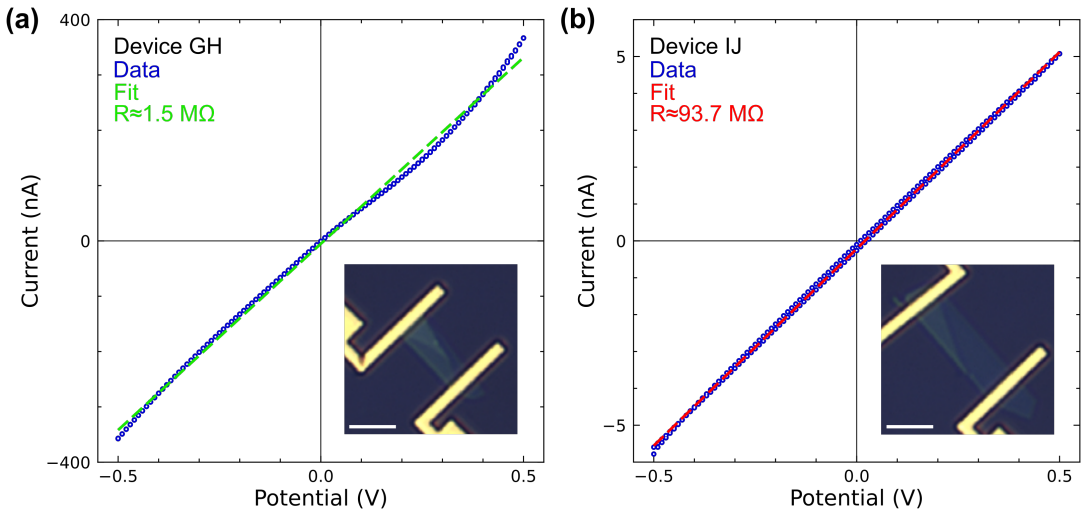

Figure 6.1: (a), (b) Measured $I-V$ characteristics (blue) and linear fits, corresponding to devices "GH" (green) and "IJ" (red). The insets show the respective devices, with the scalebars corresponding to 5 μm.

Schottky barrier behaviour. The linear fit converges to $R = 93.69 \pm 0.15$ MΩ, which is almost two orders of magnitude larger than the resistance of device "GH". Although the origin of this discrepancy is not known, it is likely to be influenced by the fact that device "GH" consists of more WS_2 layers and has a shorter channel length than "IJ".

6.2 External Quantum Efficiency

Having confirmed that the electrical contacts are working, we now turn to photocurrent generation in the devices by measuring the EQE spectra. We measure the spectra from 460 nm to 670 nm in 2 nm increments, at modulation frequency $f_r \approx 400$ Hz, with LIA filter time constant $\tau = 100$ ms and a 1 s delay for the filter to settle. Before mounting the sample, we measure laser power spectra at 25%, 50%, 75% and 100% AOTF power, to be able to calculate the EQE at these power settings with Eq. 2.3.

We first consider few-layer WS_2 device "GH", which consists of three distinct regions with different thicknesses, as shown in Fig. 3.11(a). We apply a bias voltage of 1V, set the TIA sensitivity to 100 μA/V and the initial LIA sensitivity to 20 mV (= 2 μA). We illuminate

the sample with arbitrarily oriented linear polarisation at 100% AOTF power. Figure 6.2(a) shows the spectra measured on the WS_2 device "GH" (green) and the substrate (brown), with the locations indicated by the markers in the inset. We observe that the device and substrate spectra have identical shapes with a slightly smaller magnitude for device "GH" compared to the substrate. Evidently, we measure photocurrent generated in the substrate, with the WS_2 only absorbing part of the light but not contributing to the current.

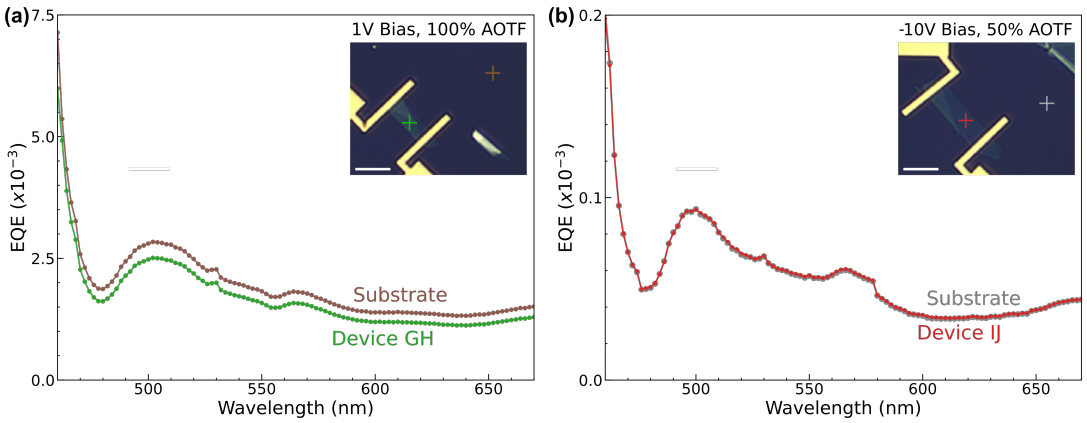

Figure 6.2: Measured EQE spectra of **(a)** WS_2 device "GH" (green) and the substrate (brown), and of **(b)** WS_2 device "IJ' (red) and the substrate (grey). The insets show optical microscope images of the devices and the surrounding regions, with the markers indicating the positions where the spectra are measured. The scale bars correspond to 5 μm.

Next, we turn our attention to device "IJ". As highlighted in Fig. 3.11(c), the flake making up this device is mainly monolayer WS_2, with a small few-layer region. Upon testing this device, we notice that we need to apply a bias with reverse polarity compared to device "GH", in order to measure a stable photocurrent signal on the LIA. Hence, to obtain the spectra shown in Fig. 6.2(b), we use a -10V bias, 10 μA/V TIA sensitivity, 5 mV (=50 nA) initial LIA sensitivity, 50% AOTF power and arbitrary linear polarisation. The spectrum of device "IJ" is shown in red and the substrate in grey, with the markers in the inset showing the positions where the spectra are acquired. The spectra are overlapping, and we clearly measure the photocurrent generated in substrate, with the WS_2 monolayer absorbing no noticeable amount of the laser light.

In principle, the 100 nm thick electrically insulating layer of silica should prevent the extraction of carriers generated in the Si substrate. It is therefore unclear why we measure a significant photocurrent signal from the substrate, though two potential causes stand out. The first is that the substrate is in contact with the sample holder's contact pads. Consequently, when applying a voltage across pins G and H, or I and J, we form a closed electrical circuit with the substrate, bypassing the wire bonds and the lithographically fabricated gold contacts. Alternatively, the thin layer of thermal oxide may be damaged in the contact fabrication stage (section 3.5). As a result, charge carriers can be extracted from the Si substrate by the contacts that caused the damage.

Curiously, we see no sign of either the B or the A exciton in the spectra measured on the WS_2 devices. Although the excitons cannot contribute to the substrate photocurrent, we should observe reduced photocurrent generated in the Si substrate due to resonant absorption in WS_2 around ~ 520 nm and ~ 620 nm for the B and A excitons, respectively. This indicates that the excitons are quenched, which can be caused by a number of factors such as electrical gating [28], structural defects and/or deformations [54, 55]. We further investigate this by measuring the reflectance spectra in the following section.

6.3 Reflectance

We use the WITec microscope with the halogen lamp and spectrometer to measure reflectance spectra and thereby investigate the observed quenching of the excitons.

Figure 6.3(a) shows the reflectance spectra, calculated with Eq. 5.1, of the WS_2 devices "GH" (green) and "IJ" (red), the substrate (grey) and a nearby uncontacted few-layer WS_2 flake (blue). The B and A exciton resonance wavelengths are indicated by the orange and magenta triangles, respectively. Figure 6.3(b) and (c) show optical microscope images of devices "GH" and "IJ", respectively, with the coloured markers indicating the locations where the spectra are measured.

We observe no signs of the A and B excitons in the reflectance spectrum of device "IJ", and it closely matches the substrate's spectrum. On the other hand, the reflectance spectrum of device "GH" features a small shoulder and a trough at the B and A exciton wavelengths, respectively. Regardless, the observed spectral shape is anomalous, particularly at wavelengths longer than

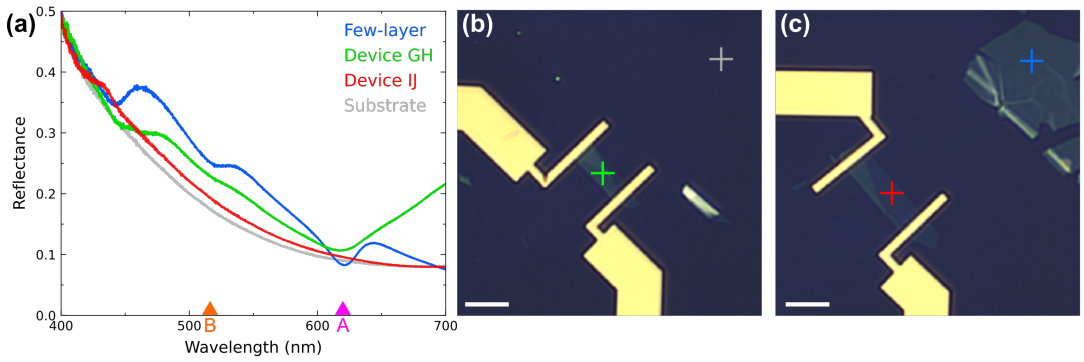

Figure 6.3: **(a)** Measured reflectance spectra of a few-layer WS_2 flake (blue), devices "GH" (green) and "IJ" (red), and the substrate (grey). **(b)**, **(c)** Optical microscope images of devices "GH" and "IJ", respectively, with the coloured markers indicating the positions the spectra are measured. The scale bars correspond to 5 μm.

the A exciton resonance wavelength, where the reflectance suddenly increases. The clearest demonstration of the excitonic influence on the optical properties is found in the spectrum of the uncontacted few-layer WS_2 flake, indicating that suppression of the excitons is caused by the gold contacts of the devices.

Notably, all three WS_2 reflectance spectra contain a feature at wavelengths shorter than the B exciton wavelength, near the ultraviolet. We attribute this to the WS_2 C exciton, which has a different origin than the A and B excitons, associated with transitions away from the K point and with a resonance wavelength around 450 nm [19, 56]. Compared to the A and B excitons, the C exciton wavelength is influenced more strongly by the number of WS_2 layers, redshifting as the thickness increases [57]. This is consistent with the data presented here, since the spectrum of monolayer "IJ" shows the feature well below 450 nm, while the resonance is observed around 450 nm for the few-layer device "GH" and the uncontacted few-layer flake.

6.4 Spatially resolved maps

In this section, we use the home-built setup to investigate local variations in the reflectance and EQE at the A exciton resonance wavelength, taken to be $\lambda = 620$ nm, by simultaneously measuring spatially resolved maps for both physical quantities. For this, we use 75% AOTF power and set the chopper wheel to modulate at $f_r \approx 400$ Hz, resulting in an average laser

power of 0.40 mW arriving at the sample. Furthermore, we use the same LIA and TIA sensitivity settings as those described in section 6.2, but change the filter time constant to $\tau = 30$ ms and delay to 300 ms to speed up the measurement.

The maps are superimposed on optical microscope images in Fig. 6.4, with the reflectance maps in the top row, panels (a)-(c), and the corresponding EQE maps in the bottom row, panels (d)-(f). The reflectance is normalised as $R = \Phi_\nu / \Phi_\nu^{\max}$, with $\Phi_\nu^{\max}$ the maximum reflected photon flux measured on the gold contacts. To improve the visibility of the WS_2 flakes, we limit the reflectance colour scales to $0 \leq R \leq 0.5$.

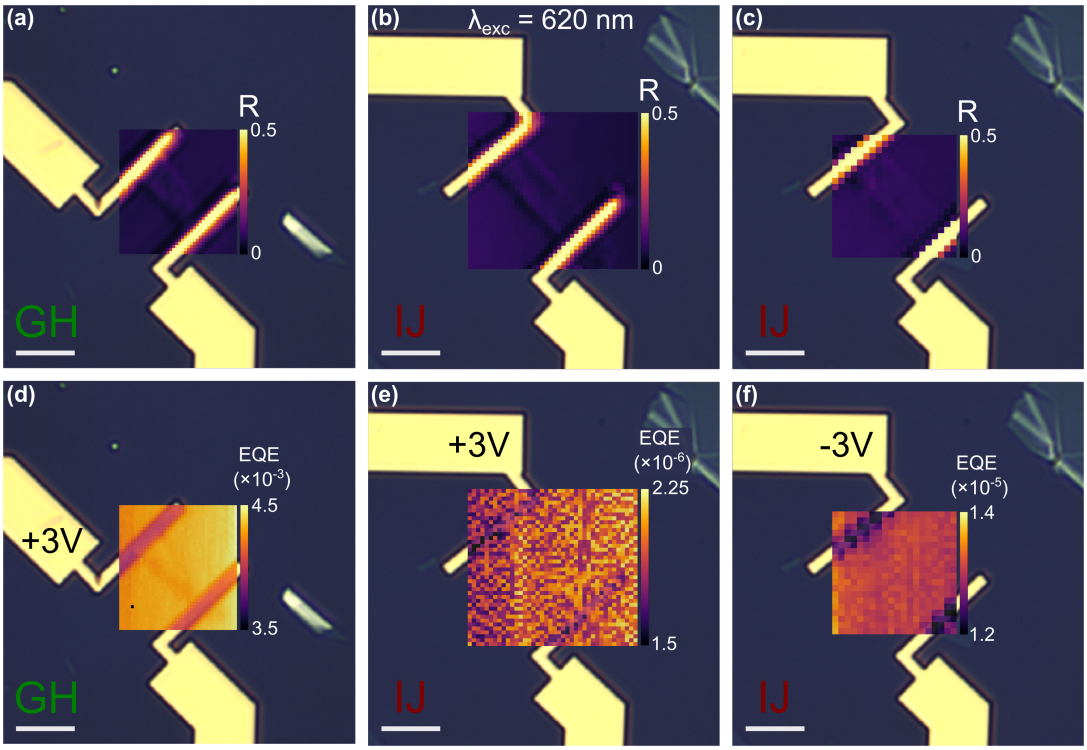

Figure 6.4: Spatially resolved maps superimposed on optical microscope images. The applied bias voltages are indicated in the EQE maps, and the scale bars correspond to 5 μm. **(a)-(c)** Reflectance maps. **(d)-(f)** EQE maps.

The maps in the first column cover an area of 9.28×9.83 μm^2 around device "GH", with 1600 pixels per map resulting in a resolution of ~ 58 nm^2/pixel. We observe no drop in the the

reflectance of the WS_2 flake compared to the substrate, as shown in panel (a). We apply a bias voltage of +3 V to extract photogenerated carriers, and use knowledge of the optical power to calculate the EQE map shown in panel (b). The EQE is very uniform, except at the gold contacts, with an average $EQE = 4.3 \cdot 10^{-3}$. The magnitude of the EQE is slightly smaller in parts of the WS_2 channel, but we attribute this mostly to thickness-dependent, non-resonant absorption. All in all, this map confirms that the photocurrent is generated in the substrate surrounding the gold contacts, instead of in the WS_2 channel.

The maps in the second column cover an area of 13.85×12.78 μm^2 in the neighbourhood of device "IJ", with 1600 pixels per map ($\sim$ 112 nm^2/pixel). We can make out the contour of the WS_2 flake in the reflectance map of panel (b), but there is no noticeable difference in reflectance of the WS_2 channel and the surrounding substrate, which points to suppression of the A exciton. Again, we apply a +3 V bias voltage to extract the photogenerated charge carriers, but in this case we only measure noise, as shown in panel (e). Apparently, a positive bias of 3 V is unfit to extract the photocarriers, which is consistent with the results discussed in section 6.2. Measuring the $I - V$ characteristic of device "IJ" for a larger range of bias voltages may provide useful insight into the polarity behaviour, but we do not explore this here.

Instead, we reverse the bias, i.e. -3 V, and map an area of 9.75×9.61 μm^2 around device "IJ", with 400 pixels per map ($\sim$ 234 nm^2/pixel), as shown in the third column, panels (c) and (f). In this case, we measure a uniform photocurrent in the substrate surrounding device "IJ", averaging $EQE = 1.3 \cdot 10^{-5}$. The quantum efficiency of device "IJ" is much smaller than device "GH". This may be the result of less efficient charge extraction from contacts I and J, in line with the $I - V$ behaviour discussed in section 6.1.

We do not further characterise the EQE, since it is clear that the photocurrent is generated in and extracted from the substrate, instead of the WS_2 channels. From the reflectance maps, we conclude that the A exciton is indeed suppressed in both of the WS_2 channels, because there is no noticeable reduction in the intensity of the back-scattered light at the resonance wavelength.

The suppression of the excitons may be the result of process-induced structural defects, stress [54, 55], or contaminants [58]. For this, Raman and PL spectroscopy are efficient and non-

destructive techniques that may be employed to investigate such defects [59]. Furthermore, the detrimental effects of the fabrication procedure may be mitigated by annealing [58, 60], and/or using the appropriate solvents to clean the sample. Specifically, Choi and co-workers [61] report adverse effects of IPA and acetone on the electrical and optical properties of TMDCs, and these solvents should therefore be avoided in future work.

Ultimately, a variety of techniques may be employed to overcome the exciton quenching described in this chapter. Besides, further research is needed to point out why photocurrent is generated in and extracted from the Si substrate. Overcoming these hurdles is paramount to address the research question by measuring the quantum efficiency of 2D WS_2 photodetectors.

Chapter 7

Summary and outlook

7.1 Summary

We have fabricated 2D WS_2 photodetectors with the goal of studying the role of excitons in photocurrent generation and the realisation of tuneable nanoscale photodetectors. Starting from a bulk WS_2 crystal, we used mechanical exfoliation to thin flakes down and obtain monolayers. Here, we have used computational techniques to find the optimal number of exfoliation steps to achieve the highest monolayer yield.

Monolayers were optically identified using the confocal WITec microscope, and we have shown that measuring the optical contrast of a WS_2 nanolayer is sufficient to determine whether it is a monolayer or not. Raman scattering and photoluminescence emission spectroscopy were used to confirm that we have reached the monolayer limit.

The 2D WS_2 flakes were deterministically transferred onto a patterned, oxidised Si substrate using a custom stamping stage utilising transparent viscoelastic stamps . The absolute positions of several WS_2 nanolayers were calculated to facilitate the design and aligned fabrication of local source and drain contacts with e-beam lithography. The substrate with the contacted WS_2 flakes was mounted on a custom sample holder an wire bonded to it, thereby completing the 2D WS_2 photodetector devices.

We have built a photocurrent mapping and spectroscopy setup to characterise the optoelectronic properties of the devices. The setup integrates a free-space laser setup and electronic

equipment with a commercial WITec microscope, and measurements are fully automated via custom Python programs. The free-space laser setup grants control over the power, wavelength and linear polarisation of the excitation laser, and the WITec's piezo stage adds control over the sample position, with 3 nm lateral positioning accuracy. Back-scattered light off the sample is captured by a fiber-coupled detector to allow for simultaneous reflection measurements. From the knife-edge measurement we conclude that the resolution of the setup is diffraction-limited.

To test the suitability of the home-built setup for the characterisation of resonant nanoscale photodetectors, we have further benchmarked it with transparent Mie-resonant Si NW arrays, designed and fabricated by Li and co-workers [3]. The "red" NW array was wire bonded to the custom sample holder, and henceforth we have measured spatially and polarisation-resolved EQE spectra and maps. With these, assuming a wavelength-independent IQE in the visible range, we have demonstrated the polarisation-dependent Mie-resonant absorption and verified our results with simulations.

We have measured reflectance maps and spectra of the NW device with the home-built setup, and compared the results with measured halogen-illumination spectra and simulations. We have obtained good agreement with the simulations, clearly demonstrating the presence of the first-order resonances in the reflectance spectra. Finally, we used the WITec with the halogen lamp and spectrometer to demonstrate the colour detection capabilities of the NW arrays.

Having fully benchmarked the home-built setup, we turned to study the 2D WS_2 photodetectors at last. From the EQE spectra, the signal appeared to be dominated by photocurrent from the Si substrate instead of the WS_2 flakes, and we observed no sign of the excitons. We measured reflectance spectra of the substrate, the two WS_2 devices, and an uncontacted WS_2 flake. From this, we concluded that the gold contacts (or fabrication process thereof) cause suppression of the excitons in the devices. Finally, we measure EQE and reflectance maps to verify that we measure photocurrent generated in the substrate and that the excitons are suppressed in the WS_2 channels.

The next step in this research is to solve the problems with the 2D WS_2 photodetectors, i.e. the unintentional exciton quenching in the contacted WS_2 flakes and the charge extraction from the Si substrate instead of in the WS_2 channels. Overcoming these obstacles is requisite for measuring the quantum efficiency of 2D WS_2 photodetectors and thereby addressing the

research question. That said, the techniques and setup presented in this thesis provide the groundwork to investigate the role of strongly bound excitons in photocurrent generation.

7.2 Outlook

There are several other outstanding challenges for the the reliable and reproducible fabrication of 2D WS_2 photodetectors. First of all, obtaining monolayer flakes with mechanical exfoliation is limited by the low monolayer yield and small lateral flake sizes. Recently, gold-assisted exfoliation has come to attention as a promising method for producing high-quality, large-area monolayers [62, 63]. Besides, the deterministic transfer procedure may be further optimised to improve the consistency. In this regard, the technique demonstrated by Zhao and co-workers [47] looking promising and should be further investigated.

The potential to use these techniques to reliably fabricate artificial heterostructures and heterojunctions on almost any substrate opens the doors for countless conceivable optoelectronic devices. In the near term, transparent, flexible, and/or wearable devices may become a reality, owing to the natural transparency of 2D materials, combined with a significant Young's modulus and high breaking strength [64]. The first prototypes have already been achieved by transferring nanolayers to flexible substrates, showing robust performance upon repeated straining [54, 65–67]. In that regard, another avenue to explore is strain-tuning. The exciton resonances can be reversibly redshifted by applying strain [68, 69]. Hence, active modulation of excitonic photocurrent may be achieved by using computer-controlled, motorised actuators to apply the strain.

Additionally, in future work, electrostatic gating can readily be incorporated in the device architecture presented in this thesis. The resulting FET scheme may be used to actively tune the relative carrier densities in the WS_2 flakes and even reversibly quench the excitons [28], adding a desirable degree of freedom to study the role of excitons in photocurrent generation. A diverse array of 2D TMDC photodetectors with FET architectures have already been demonstrated in literature [25, 26, 54, 67, 70] and can, for instance, be used to drastically improve the excitonic absorption efficiency [20]. Regardless, further device optimisations are needed before 2D TMDC FETs can become competitive with conventional materials, necessitating a deeper understanding of the exciton dissociation mechanisms for efficient photocurrent generation.

Bibliography

1. Buscema, M. *et al.* Photocurrent generation with two-dimensional van der Waals semiconductors. *Chemical Society Reviews* **44,** 3691–3718 (2015).
2. Cao, L., Fan, P., Barnard, E. S., Brown, A. M. & Brongersma, M. L. Tuning the color of silicon nanostructures. *Nano Letters* **10,** 2649–2654 (2010).
3. Li, Q., Van de Groep, J., Wang, Y., Kik, P. G. & Brongersma, M. L. Transparent multispectral photodetectors mimicking the human visual system. *Nature Communications* **10,** 1–8 (2019).
4. Yi, S. *et al.* Subwavelength angle-sensing photodetectors inspired by directional hearing in small animals. *Nature Nanotechnology* **13,** 1143–1147 (2018).
5. Van de Groep, J. & Brongersma, M. L. Metasurface Mirrors for External Control of Mie Resonances. *Nano Letters* **18,** 3857–3864 (2018).
6. Fox, M. *Optical Properties of Solids* ISBN: 978-0-19-957336-3 (Oxford University Press, 2010).
7. Novoselov, K. S. *et al.* Two-dimensional atomic crystals. *Proceedings of the National Academy of Sciences of the United States of America* **102,** 10451–10453 (2005).
8. Mak, K. F., Lee, C., Hone, J., Shan, J. & Heinz, T. F. Atomically thin MoS_2: A new direct-gap semiconductor. *Physical Review Letters* **105,** 2–5 (2010).
9. Wang, G. *et al.* Colloquium: Excitons in atomically thin transition metal dichalcogenides. *Reviews of Modern Physics* **90,** 21001 (2018).
10. Zhu, B., Chen, X. & Cui, X. Exciton binding energy of monolayer WS_2. *Scientific Reports* **5** (2015).

11. Sze, S. M. & Kwok, K. N. *Physics of Semiconductor Devices* ISBN: 978-0-471-14323-9 (John Wiley & Sons, 2007).

12. Mounet, N. *et al.* Two-dimensional materials from high-throughput computational exfoliation of experimentally known compounds. *Nature Nanotechnology* **13,** 246–252 (2018).

13. Chhowalla, M. *et al.* The chemistry of two-dimensional layered transition metal dichalcogenide nanosheets. *Nature Chemistry* **5,** 263–275 (2013).

14. Manzeli, S., Ovchinnikov, D., Pasquier, D., Yazyev, O. V. & Kis, A. 2D transition metal dichalcogenides. *Nature Reviews Materials* **2,** 1–15 (2017).

15. Terrones, H., López-Urías, F. & Terrones, M. Novel hetero-layered materials with tunable direct band gaps by sandwiching different metal disulfides and diselenides. *Scientific Reports* **3** (2013).

16. Jariwala, D., Sangwan, V. K., Lauhon, L. J., Marks, T. J. & Hersam, M. C. Emerging device applications for semiconducting two-dimensional transition metal dichalcogenides. *ACS Nano* **8,** 1102–1120 (2014).

17. Mueller, T. & Malic, E. Exciton physics and device application of two-dimensional transition metal dichalcogenide semiconductors. *2D Materials and Applications* **2,** 1–12 (2018).

18. Chernikov, A. *et al.* Exciton Binding Energy and Nonhydrogenic Rydberg Series in Monolayer WS_2. *Physical Review Letters* **113,** 076802 (2014).

19. Li, Y. *et al.* Measurement of the optical dielectric function of monolayer transition-metal dichalcogenides: MoS_2, $MoSe_2$, WS_2, and WSe_2. *Physical Review B - Condensed Matter and Materials Physics* **90,** 1–6 (2014).

20. Epstein, I. *et al.* Near-unity light absorption in a monolayer WS_2 van der waals heterostructure cavity. *Nano Letters* **20,** 3545–3552 (2020).

21. Novoselov, K. S., Mishchenko, A., Carvalho, A. & Castro Neto, A. H. 2D materials and van der Waals heterostructures. *Science* **353** (2016).

22. Haastrup, S., Latini, S., Bolotin, K. & Thygesen, K. S. Stark shift and electric-field-induced dissociation of excitons in monolayer MoS_2 and hBN/ MoS_2 heterostructures. *Physical Review B* **94,** 1–5 (2016).

23. Massicotte, M. *et al.* Dissociation of two-dimensional excitons in monolayer WSe 2. *Nature communications* **9,** 1–7 (2018).

24. Zhang, Q. *et al.* Strain Relaxation of Monolayer WS_2 on Plastic Substrate. *Advanced Functional Materials* **26,** 8707–8714 (2016).

25. Hwan Lee, S. *et al.* High-performance photocurrent generation from two-dimensional WS_2 field-effect transistors. *Applied Physics Letters* **104** (2014).

26. Yang, Y. *et al.* Tunable Polarity Behavior and High-Performance Photosensitive Characteristics in Schottky-Barrier Field-Effect Transistors Based on Multilayer WS_2. *ACS Applied Materials and Interfaces* **10,** 2745–2751 (2018).

27. Wang, Q. *et al.* High-Energy Gain Upconversion in Monolayer Tungsten Disulfide Photodetectors. *Nano Letters* **19,** 5595–5603 (2019).

28. Van de Groep, J. *et al.* Exciton resonance tuning of an atomically thin lens. *Nature Photonics* **14,** 426–430 (2020).

29. Frisenda, R., Molina-Mendoza, A. J., Mueller, T., Castellanos-Gomez, A. & Van Der Zant, H. S. Atomically thin p-n junctions based on two-dimensional materials. *Chemical Society Reviews* **47,** 3339–3358 (2018).

30. Liu, F. Mechanical exfoliation of large area 2D materials from vdW crystals. *Progress in Surface Science,* 100626 (2021).

31. K. S. Novoselov and A. K. Geim and S. V. Morozov and D. Jiang and Y. Zhang and S. V. Dubonos and I. V. Grigorieva and A. A. Firsov. Electric Field Effect in Atomically Thin Carbon Films. *Science* **306,** 666–669 (2016).

32. Ottaviano, L. *et al.* Mechanical exfoliation and layer number identification of MoS_2 revisited. *2D Materials* **4** (2017).

33. Bohr, J. Adhesive tape exfoliation: Why it works for graphene. *Epl* **109** (2015).

34. Novoselov, K. S. Nobel Lecture: Graphene: Materials in the Flatland. *Reviews of Modern Physics* **83,** 837–849 (2011).

35. Benameur, M. M. *et al.* Visibility of dichalcogenide nanolayers. *Nanotechnology* **22** (2011).

36. Hsu, C. *et al.* Thickness-Dependent Refractive Index of 1L, 2L, and 3L MoS_2, $MoSe_2$, WS_2, and WSe_2. *Advanced Optical Materials* **7** (2019).

37. Molas, M. R., Nogajewski, K., Potemski, M. & Babiński, A. Raman scattering excitation spectroscopy of monolayer WS_2. *Scientific Reports* **7,** 5036 (2017).

38. Berkdemir, A. *et al.* Identification of individual and few layers of WS_2 using Raman Spectroscopy. *Scientific Reports* **3,** 1–8 (2013).

39. Qiao, S., Yang, H., Bai, Z., Peng, G. & Zhang, X. Identifying the number of WS_2 layers via Raman and photoluminescence spectrum. *Advances in Engineering Research* **141,** 1408–1413 (2017).

40. Tonndorf, P. *et al.* Photoluminescence emission and Raman response of monolayer MoS_2, $MoSe_2$, and WSe_2. *Optics Express* **21,** 4908–4916 (2013).

41. Das, S., Kallatt, S., Abraham, N. & Majumdar, K. Gate-tunable trion switch for excitonic device applications. *Physical Review B* **101,** 81413 (2020).

42. Jadczak, J. *et al.* Probing of free and localized excitons and trions in atomically thin WSe_2, WS_2, $MoSe_2$ and MoS_2 in photoluminescence and reflectivity experiments. *Nanotechnology* **28,** 395702 (2017).

43. Chow, P. K. *et al.* Defect-induced photoluminescence in monolayer semiconducting transition metal dichalcogenides. *ACS Nano* **9,** 1520–1527 (2015).

44. Tebyetekerwa, M. *et al.* Mechanisms and Applications of Steady-State Photoluminescence Spectroscopy in Two-Dimensional Transition-Metal Dichalcogenides. *ACS Nano* **14,** 14579–14604 (2020).

45. Rosenberger, M. R., Chuang, H. J., McCreary, K. M., Li, C. H. & Jonker, B. T. Electrical Characterization of Discrete Defects and Impact of Defect Density on Photoluminescence in Monolayer WS_2. *ACS Nano* **12,** 1793–1800 (2018).

46. Plechinger, G. *et al.* Identification of excitons, trions and biexcitons in single-layer WS_2. *Physica Status Solidi - Rapid Research Letters* **9,** 457–461 (2015).

47. Zhao, Q., Wang, T., Ryu, Y. K., Frisenda, R. & Castellanos-Gomez, A. An inexpensive system for the deterministic transfer of 2D materials. *Journal of Physics: Materials* **3,** 016001 (2020).

48. Castellanos-Gomez, A. *et al.* Deterministic transfer of two-dimensional materials by all-dry viscoelastic stamping. *2D Materials* **1,** 1–20 (2014).

49. *Principles of lock-in detection and the state of the art* Zurich Instruments (2016).

50. *Model SR830 DSP Lock-In Amplifier Manual* version 2.5. Stanford Research Systems (2011).

51. *SuperK SELECT Product Guide* NKT Photonics (2021).

52. Liu, J.-M. *Principles of Photonics* ISBN: 978-1-107-16428-4 (Cambridge University Press, 2016).

53. Novotny, L. & Hecht, B. *Principles of Nano-Optics* ISBN: 978-0-511-16811-6 (Cambridge University Press, 2006).

54. Aji, A. S., Solís-Fernández, P., Ji, H. G., Fukuda, K. & Ago, H. High Mobility WS_2 Transistors Realized by Multilayer Graphene Electrodes and Application to High Responsivity Flexible Photodetectors. *Advanced Functional Materials* **27,** 1–10 (2017).

55. Kim, C. *et al.* Fermi Level Pinning at Electrical Metal Contacts of Monolayer Molybdenum Dichalcogenides. *ACS Nano* **11,** 1588–1596 (2017).

56. Niu, Y. *et al.* Thickness-dependent differential reflectance spectra of monolayer and few-layer MoS_2, $MoSe_2$, WS_2 and WSe_2. *Nanomaterials* **8** (2018).

57. Zhao, W. *et al.* Evolution of Electronic Structure in Atomically Thin Sheets of WS_2 and WSe_2. *ACS Nano* **7,** 791–797 (2013).

58. Frisenda, R. *et al.* Recent progress in the assembly of nanodevices and van der Waals heterostructures by deterministic placement of 2D materials. *Chemical Society Reviews* **47,** 53–68 (2018).

59. Wu, Z. *et al.* Defects as a factor limiting carrier mobility in WSe_2: A spectroscopic investigation. *Nano Research* **9,** 3622–3631 (2016).

60. Bandyopadhyay, A. S., Saenz, G. A. & Kaul, A. B. Role of metal contacts and effect of annealing in high performance 2D WSe_2 field-effect transistors. *Surface and Coatings Technology* **381** (2020).

61. Choi, J., Zhang, H., Du, H. & Choi, J. H. Understanding Solvent Effects on the Properties of Two-Dimensional Transition Metal Dichalcogenides. *ACS Applied Materials and Interfaces* **8,** 8864–8869 (2016).

62. Velický, M. *et al.* Mechanism of Gold-Assisted Exfoliation of Centimeter-Sized Transition-Metal Dichalcogenide Monolayers. *ACS Nano* **12,** 10463–10472 (2018).

63. Huang, Y. *et al.* Universal mechanical exfoliation of large-area 2D crystals. *Nature Communications* **11** (2020).

64. Bertolazzi, S., Brivio, J. & Kis, A. Stretching and breaking of ultrathin MoS_2. *ACS Nano* **5,** 9703–9709 (2011).

65. Lee, G. H. *et al.* Flexible and transparent MoS_2 field-effect transistors on hexagonal boron nitride-graphene heterostructures. *ACS Nano* **7,** 7931–7936 (2013).

66. Pak, S. *et al.* Strain-Engineering of Contact Energy Barriers and Photoresponse Behaviors in Monolayer MoS_2 Flexible Devices. *Advanced Functional Materials* **30,** 1–7 (2020).

67. Georgiou, T. *et al.* Vertical field-effect transistor based on graphene-WS_2 heterostructures for flexible and transparent electronics. *Nature Nanotechnology* **8,** 100–103 (2013).

68. He, K., Poole, C., Mak, K. F. & Shan, J. Experimental demonstration of continuous electronic structure tuning via strain in atomically thin MoS_2. *Nano Letters* **13,** 2931–2936 (2013).

69. Carrascoso, F., Lin, D. Y., Frisenda, R. & Castellanos-Gomez, A. Biaxial strain tuning of interlayer excitons in bilayer MoS_2. *JPhys Materials* **3** (2020).

70. Massicotte, M. *et al.* Picosecond photoresponse in van der Waals heterostructures. *Nature Nanotechnology* **11,** 42–46 (2016).

Acknowledgements

Throughout the year, I have received a great deal of assistance and support. First of all, thanks to Jorik van de Groep for the opportunity to do such an exciting project in the 2D Nanophotonics lab, and for his great supervision. Many thanks to Ludovica Guarneri for her guidance, training me on the setup, e-beam lithography in the AMOLF NanoLab and last but not least, her invaluable feedback on this thesis. Thanks also to Kian Goeloe for the collaboration, especially in refining the exfoliation and stamping techniques, but also for all the time spent searching monolayers and helping with the Python programs. I would like to acknowledge the technical staff at Science Park, particularly Gerrit Hardeman for his expertise in setting up the communication with the lab equipment, Hans Ellermeijer for fabricating multiple custom parts, Guoyong Zhang for training me on the wire bonder, and Yingkai Huang for providing me with additional WS_2 and WSe_2 crystals. Furthermore, I would like to acknowledge Qitong Li from Stanford University for providing me with the Si NW array sample, as well as for supplying figures from his excellent paper. Thanks also to Marco van der Laan for being my go-to remote lab partner and for his contributions to discussions. Last but not least, many thanks to Mathilda and my family for all the support.